The Astrophysical Journal, 593:96–114, 2003 August 10

X-RAY FLUCTUATION POWER SPECTRAL DENSITIES OF SEYFERT 1 GALAXIES

A. Markowitz,[1] R. Edelson,[1] S. Vaughan,[2] P. Uttley,[3] I. M. George,[4,5] R. E. Griffiths,[6] S. Kaspi,[7] A. Lawrence,[8] I. McHardy,[3] K. Nandra,[5,9] K. Pounds,[10] J. Reeves,[10] N. Schurch,[10,11] and R. Warwick[10]

Received 2002 September 20; accepted 2003 March 12

ABSTRACT

By combining complementary monitoring observations spanning long, medium, and short timescales, we have constructed power spectral densities (PSDs) of six Seyfert 1 galaxies. These PSDs span $\gtrsim 4$ orders of magnitude in temporal frequency, sampling variations on timescales ranging from tens of minutes to over a year. In at least four cases, the PSD shows a "break," a significant departure from a power law, typically on timescales of the order of a few days. This is similar to the behavior of Galactic X-ray binaries (XRBs), lower mass compact systems with breaks on timescales of seconds. NGC 3783 shows tentative evidence for a doubly broken power law, a feature that until now has been seen only in the (much better defined) PSDs of low-state XRBs. It is also interesting that (when one previously observed object is added to make a small sample of seven) an apparently significant correlation is seen between the break timescale T and the putative black hole mass $M_{\rm BH}$, while none is seen between break timescale and luminosity. The data are consistent with the linear relation $T = M_{\rm BH}/10^{6.5}\ M_{\odot}$; extrapolation over 6–7 orders of magnitude is in reasonable agreement with XRBs. All of this strengthens the case for a physical similarity between Seyfert 1 galaxies and XRBs.

Subject headings: galaxies: active — galaxies: Seyfert — X-rays: galaxies

1. INTRODUCTION

Early X-ray observations of Seyfert 1 galaxies showed strong, aperiodic X-ray variability, evidence that the X-rays are emitted in close proximity to the central black hole. Because its properties are so well studied and understood (e.g., Priestley 1981), the fluctuation power spectral density (PSD) is a common tool for temporal analysis. The first Seyfert 1 PSDs were measured with the *EXOSAT* long-looks. These established the red-noise nature of Seyfert 1 galaxy variability over the timescales of $\sim 2 \times 10^{-3}$ to $\sim 2 \times 10^{-5}$ Hz (Lawrence et al. 1987; McHardy & Czerny 1987; Lawrence & Papadakis 1993; Green, McHardy, & Lehto 1993).

Edelson & Nandra (1999; hereafter EN99) completed the first systematic broadband PSD study using a series of contemporaneous, evenly sampled *Rossi X-Ray Timing Explorer* (*RXTE*) observations of NGC 3516 to measure a PSD spanning over three decades of temporal frequency (4×10^{-8} to 7×10^{-4} Hz). This yielded the first clear evidence of a break in the power-law PSD at $\sim 4 \times 10^{-7}$ Hz (~ 1 month) and an intriguing similarity to the PSDs of X-ray binaries (XRBs; see also McHardy 1988; Papadakis & McHardy 1995).

Pounds et al. (2001) applied a similar sampling pattern to the narrow-line (soft-spectrum) Seyfert 1 Ark 564. The PSD showed a higher cutoff frequency, $\sim 9 \times 10^{-7}$ Hz (corresponding to ~ 2 weeks), which Pounds et al. (2001) argued was consistent with such objects having lower mass black holes emitting at a higher fraction of the Eddington rate. Uttley, McHardy, & Papadakis (2002, hereafter UMP02) confirmed the break in the PSD of NGC 3516 and additionally studied three other Seyfert galaxies. The Seyfert 1 MCG -6-30-15 and the Seyfert 2 NGC 5506 both showed breaks at $\sim 5 \times 10^{-5}$ Hz (corresponding to ~ 6 hr), but no clear break was seen in the Seyfert 1 NGC 5548.

Given that the above frequency breaks depend on the model used to fit the PSD as well as the analysis method, a more systematic picture of Seyfert 1 PSDs can be attained with uniform analysis and models. To accomplish this, we have applied the EN99 observing technique to a sample of six Seyfert 1 galaxies, as given in Table 1. These monitoring data were used to construct high dynamic range PSDs and search for departures from power-law behavior. The observations, data reduction, and resulting light curves are described in § 2. The PSD measurement and modeling are discussed in § 3. We employ the Monte Carlo technique of UMP02 to quantify errors and account for red-noise leak and aliasing. The model-fitting results and evidence for a break in the power-law PSD are given in § 4. The results were then combined with the MCG -6-30-15 result of UMP02 to create a PSD survey of seven Seyfert 1 galaxies. The physical implications of this break are discussed and a comparison with the PSD and other variability properties

[1] Department of Astronomy, University of California, Los Angeles, CA 90095-1562; agm@astro.ucla.edu,rae@astro.ucla.edu.

[2] Institute of Astronomy, Madingley Road, Cambridge, CB3 0HA, UK; sav@ast.cam.ac.uk.

[3] Department of Physics and Astronomy, University of Southampton, Southampton, SO17 1BJ, UK; pu@astro.soton.ac.uk.

[4] Joint Center for Astrophysics, Physics Department, University of Maryland, Baltimore County, 1000 Hilltop Circle, Baltimore, MD 21250.

[5] Laboratory for High Energy Astrophysics, NASA Goddard Space Flight Center, Code 662, Greenbelt, MD 20771.

[6] Department of Physics, Carnegie Mellon University, Pittsburgh, PA 15213-3890.

[7] School of Physics and Astronomy and the Wise Observatory, Raymond and Beverly Sackler Faculty of Exact Sciences, Tel Aviv University, Tel Aviv 69978, Israel.

[8] Institute for Astronomy, University of Edinburgh, Royal Observatory, Blackford Hill, Edinburgh EH9 3HJ, UK.

[9] Astrophysics Group, Imperial College, Blackett Laboratory, Prince Consort Road, London SW7 2BW, UK.

[10] X-Ray Astronomy Group, University of Leicester, Leicester LE1 7RH, UK.

[11] Current address: Department of Physics, Carnegie Mellon University, Pittsburgh, PA 15213-3890.

TABLE 1

Source Parameters for the Seyfert Galaxies

Source Name (1)	$L_{2-10\,\mathrm{keV}}$ [log10 (erg s^{-1})] (2)	z (3)	FWHM Hβ (km s^{-1}) (4)	Γ_{2-10} (5)
Frl 9	43.97	0.047	5900	2.18
NGC 5548	43.50	0.017	5610	1.79
Ark 564	43.49	0.024	720	2.68
NGC 3783	43.22	0.010	2980	1.77
NGC 3516	42.86	0.009	6800	1.60
NGC 4151	42.62	0.003	5000	1.65

Note.—Targets are ranked by unabsorbed 2–10 keV luminosity, listed in col. (2). Luminosities were calculated with the online W3PIMMS tool and using the long-term mean *RXTE* count rates and the X-ray photon indices, assuming a cold absorption column equal to the Galactic column (for NGC 4151, a column density 230 times the Galactic column was used; see Schurch & Warwick 2002), and calculated assuming $H_0 = 75$ km s^{-1} Mpc^{-1} and $q_0 = 0.5$. Redshifts (col. [3]) were obtained from the NED database. Hβ values (col. [4]) were taken from Turner et al. 1999; see references therein. The photon indices in col. (5) were obtained from the Tartarus database, derived from a simple power-law fit covering the 2–10 keV bandpass, except for Ark 564, from a spectral fit by Vaughan et al. 1999, NGC 3783, from a spectral fit to *Chandra* data by Kaspi et al. 2001, and NGC 4151, from a spectral fit to *XMM-Newton* data by Schurch & Warwick 2002.

of XRBs is made in § 5. A brief summary of these results is given in § 6.

2. OBSERVATIONS AND DATA REDUCTION

2.1. *Sampling*

The sampling pattern employed herein (based on EN99) covers complementary long, medium, and short timescales with progressively shorter and denser relatively even sampling. This makes it possible to construct a PSD that covers the maximum temporal frequency range while minimizing the amount of telescope time needed. It also requires the assumption that the variations are stationary or at most mildly nonstationary; this assumption is tested in § 4.4. The specific sampling patterns are described below and tabulated in Table 2.

Long (*months to year*) *timescales*.—For all six targets, *RXTE* obtained nearly even sampling every ~4.3 days (~64 orbits) over a period of $\gtrsim$3 yr. In NGC 5548, observations in 1996–1999 every ~14 days were also included. Observations lasted only a fraction of an orbit (~1 ks) in all cases.

Medium (*day to weeks*) *timescales*.—For four of the objects, medium-timescale sampling was obtained with *RXTE* by observing once every other orbit (3.2 hr) for 256 epochs, spanning 34 days. For NGC 3783, this sampling was once every other orbit for 151 epochs (~20 days), and for NGC 3516, it was once every eight orbits for 136 days. Again, ~1 ks samples were used.

Short (*hours*) *timescales*.—Quasi-continuous (~60–300 ks) observations were obtained with *XMM-Newton* (for NGC 5548 and NGC 4151), *Chandra* (NGC 3783), and *RXTE* (NGC 3516). These observations were interrupted only by periods of increased particle backgrounds (for *RXTE* and occasionally *XMM-Newton*) and were sensitive to $\gtrsim$3% variations on timescales as short as ~1 ks. The other two sources (Ark 564 and Frl 9) had only short (<35 ks) uninterrupted *XMM-Newton* observations.

2.2. *RXTE Data Reduction*

All of the long- and medium-term data were obtained with *RXTE* using similar sampling patterns; data reduction proceeded in a similar fashion for all these observations, as

TABLE 2

Sampling Parameters

Source Name (1)	Timescale (2)	Instrument (3)	MJD Date Range (4)	ΔT_{samp} (5)	Number of Points (6)	Fraction Missing (%) (7)	μ (8)	F_{var} (%) (9)
Frl 9	Long	*RXTE*	51180.59–52311.18	4.27 days	266	7.9	1.54	39.2 ± 1.8
	Medium	*RXTE*	52144.88–52178.97	3.2 hr	258	13.2	2.09	14.7 ± 0.7
NGC 5548	Long	*RXTE*	50208.07–52417.02	14 days	158	0.0	4.82	34.5 ± 0.9
	Medium	*RXTE*	52091.70–52125.40	3.2 hr	255	8.2	4.51	26.3 ± 1.2
	Short	*XMM*	52097.68–52098.63	900 s	93	0.0	2.99	5.3 ± 0.4
Ark 564	Long	*RXTE*	51179.58–52310.19	4.27 days	266	7.9	1.73	29.2 ± 1.3
	Medium	*RXTE*	51694.86–51726.51	3.2 hr	239	13.0	2.00	34.9 ± 1.7
NGC 3783	Long	*RXTE*	51180.55–52311.25	4.27 days	266	9.4	7.09	22.3 ± 1.0
	Medium	*RXTE*	51960.17–51980.05	3.2 hr	151	7.9	5.65	12.8 ± 0.8
	Short	*Chandra*	51964.80–51966.74	2000 s	84	0.0	0.39	12.3 ± 0.9
	Short	*Chandra*	51967.40–51969.38	2000 s	84	0.0	0.39	11.9 ± 0.9
	Short	*Chandra*	51978.04–51979.94	2000 s	84	0.0	0.41	11.5 ± 0.9
	Short	*Chandra*	51999.17–52001.11	2000 s	84	0.0	0.58	15.1 ± 1.2
	Short	*Chandra*	52086.43–52088.38	2000 s	84	0.0	0.49	13.5 ± 1.0
NGC 3516	Long	*RXTE*	50523.03–51593.40	4.27 days	252	15.1	3.77	37.8 ± 1.8
	Medium	*RXTE*	50523.03–50659.09	12.8 hr	256	22.7	4.21	28.0 ± 1.4
	Short	*RXTE*	50590.01–50594.22	1200 s	304	15.1	3.85	7.6 ± 0.3
	Short	*RXTE*	50916.34–50919.67	1200 s	241	29.1	5.09	10.4 ± 0.6
NGC 4151	Long	*RXTE*	51179.56–51964.65	4.27 days	185	6.0	14.86	38.1 ± 2.0
	Medium	*RXTE*	51870.60–51904.79	3.2 hr	259	11.2	7.43	18.4 ± 0.9
	Short	*XMM*	51900.48–51901.14	1100 s	53	0.0	3.04	7.8 ± 0.8

Note.—Targets are ranked by 2–10 keV luminosity. Col. (5), ΔT_{samp}, is the sampling interval. Col. (8), μ, is the mean count rate. *RXTE* count rates are per 1 PCU.

well as the two NGC 3516 long-looks. These data were obtained with the proportional counter array (PCA), which consists of five identical collimated proportional counter units (PCUs; Swank 1998). For simplicity, data were collected only from those PCUs that did not suffer from repeated breakdown during on-source time (PCUs 0, 1, and 2 prior to 1998 December 23; PCUs 0 and 2 from 1998 December 23 until 2000 May 12; PCU 2 only after 2000 May 12). Count rates quoted in this paper are normalized to 1 PCU. Only PCA STANDARD-2 data were considered. The data were reduced using standard extraction methods and FTOOLS version 4.2 software. Data were rejected if they were gathered less than 10° from the Earth's limb, if they were obtained within 30 minutes after the satellite's passage through the South Atlantic Anomaly (SAA), if ELECTRON0 was greater than 0.1 (ELECTRON2 after 2000 May 12), or if the satellite's pointing offset was greater than 0°.02.

Because the PCA has no simultaneous background monitoring capability, background data were estimated by using PCABACKEST version 2.1b to generate model files based on the particle-induced background, SAA activity, and the diffuse X-ray background. This background subtraction is the dominant source of systematic error in *RXTE* active galactic nucleus (AGN) monitoring data (e.g., EN99). Counts were extracted only from the topmost PCU layer to maximize the signal-to-noise ratio. All of the targets were faint (<40 counts s^{-1} PCU^{-1}), so the applicable "L7-240" background models were used. Because the PCU gain settings have changed three times since launch, the count rates were rescaled to a common gain epoch (gain epoch 3) by calibrating with several public archive Cas A observations. Light curves binned to 16 s were generated for all targets over the 2–10 keV bandpass, where the PCA is most sensitive and the systematic errors and background are best quantified. The data were then further binned as listed in Table 2 column (5); bins with less than 10 flux points were excluded from analysis. Standard errors were derived from the data in each orbital bin. Further details of *RXTE* data reduction can be found in EN99.

2.3. *XMM-Newton Observations and Data Reduction*

2.3.1. *NGC 5548*

XMM-Newton observed NGC 5548 for 97 ks during revolution 290 from 2001 July 09 16:08:04 UT to 2001 July 10 18:06:21 UT. Data from the high-throughput European Photon Imaging Camera (EPIC) instruments, the *pn* (Strüder et al. 2001), and two MOS cameras (Turner et al. 2001) were used. The medium filters were used. Because of their higher count rate and signal-to-noise ratio, only the *pn* data were used for PSD analysis; the MOS data are henceforth ignored. The *pn* camera was operated in Small Window mode; the readout time was 5.7 ms.

A standard reduction of the raw *pn* data was done using the Science Analysis System. This involved the subtraction of hot, dead, or flickering pixels, removal of events due to electronic noise, and correction of event energies for charge transfer losses. The patterns used were 0–4 (single and double pixel events). The extraction region used was a circle of radius 40″. The core was not excluded because the level of pileup was fairly small (<2%). The background count rate was extracted in 250 s bins using the same size region in the same chip but off-source (>1′). Solar flare activity caused a tremendous increase in the soft proton flux during the final 13.5 ks, rendering that section of data useless for PSD analysis. This resulted in 83.5 ks of useful data; a background-subtracted light curve over the 2–10 keV band was initially extracted in 1 s bins. In a red-noise PSD derived from a continuous light curve, the power amplitude at the highest temporal frequencies will be dominated by the constant power level contributed by Poisson noise, $P_{\rm Psn}$, instead of the intrinsic source variability. To ensure a high variability-to-noise PSD with the intrinsic source variability power being greater than the Poisson noise power at all frequencies sampled, the data were binned at the timescale where the intrinsic variability was equal to $P_{\rm Psn}$; in the case of the NGC 5548 data, this timescale was 900 s.

2.3.2. *NGC 4151*

NGC 4151 was observed by *XMM-Newton* for 100 ks during revolution 190 from 2000 December 22 02:48:22 UT to 2000 December 23 05:29:59 UT. Because of two 8 ks gaps that would have seriously complicated the PSD analysis, only the final 57 ks was used. Again, the medium filter was used for all three EPIC instruments, which were operated in Full Frame mode. Data reduction over the 2–10 keV band proceeded in a similar manner to that of NGC 5548; again, because of their higher count rate and signal-to-noise ratio, the *pn* data only were used for PSD analysis. The patterns used were 0–4 (single and double pixel events). The area of source extraction was a circle of radius 30″; background count rates were extracted over a region 4.4 times as large. Because of the low source flux, photon pileup was not an issue. Background-subtracted light curves initially extracted in 1 s bins were rebinned to 1100 s.

2.4. *Chandra Observations and Data Reduction for NGC 3783*

Chandra observed NGC 3783 for 170 ks each of five times during 2001 March–June using the High Energy Transmission Grating Spectrometer (HETGS; e.g., Markert et al. 1994) with the Advanced CCD Imaging Spectrometer (e.g., Nousek et al. 1998; Plucinsky et al. 2003) as the detector. The data were reduced using CIAO software version 2.1.2 and its associated calibration data. Photons in the 2–10 keV band were extracted from the MEG and HEG dispersed first orders because the zeroth order in the HETGS images of NGC 3783 suffers from heavy photon pileup. The extraction width on the dispersed spectrum was done with the CIAO default of 4″.78. NGC 3783 is a pointlike source, and no extended circumnuclear emission was detected; the working assumption was that all photons in the dispersive arms were from the central source. The background count rate was negligible (several orders of magnitude smaller than the signal) in the dispersed arms and was not subtracted. Further details of the *Chandra* data reduction can be found in Kaspi et al. (2002). Light curves initially extracted in bins of 32.41 s were truncated to equal lengths of 167.6 ks and rebinned to 2000 s for a total of 84 data points in each light curve.

2.5. *The Light Curves*

The resulting light curves are shown in Figures 1–4. Figure 1 shows the long- and medium-term data from *RXTE* monitoring, with the short-term NGC 3516 *RXTE* long-looks included and the locations of the *XMM-Newton* and

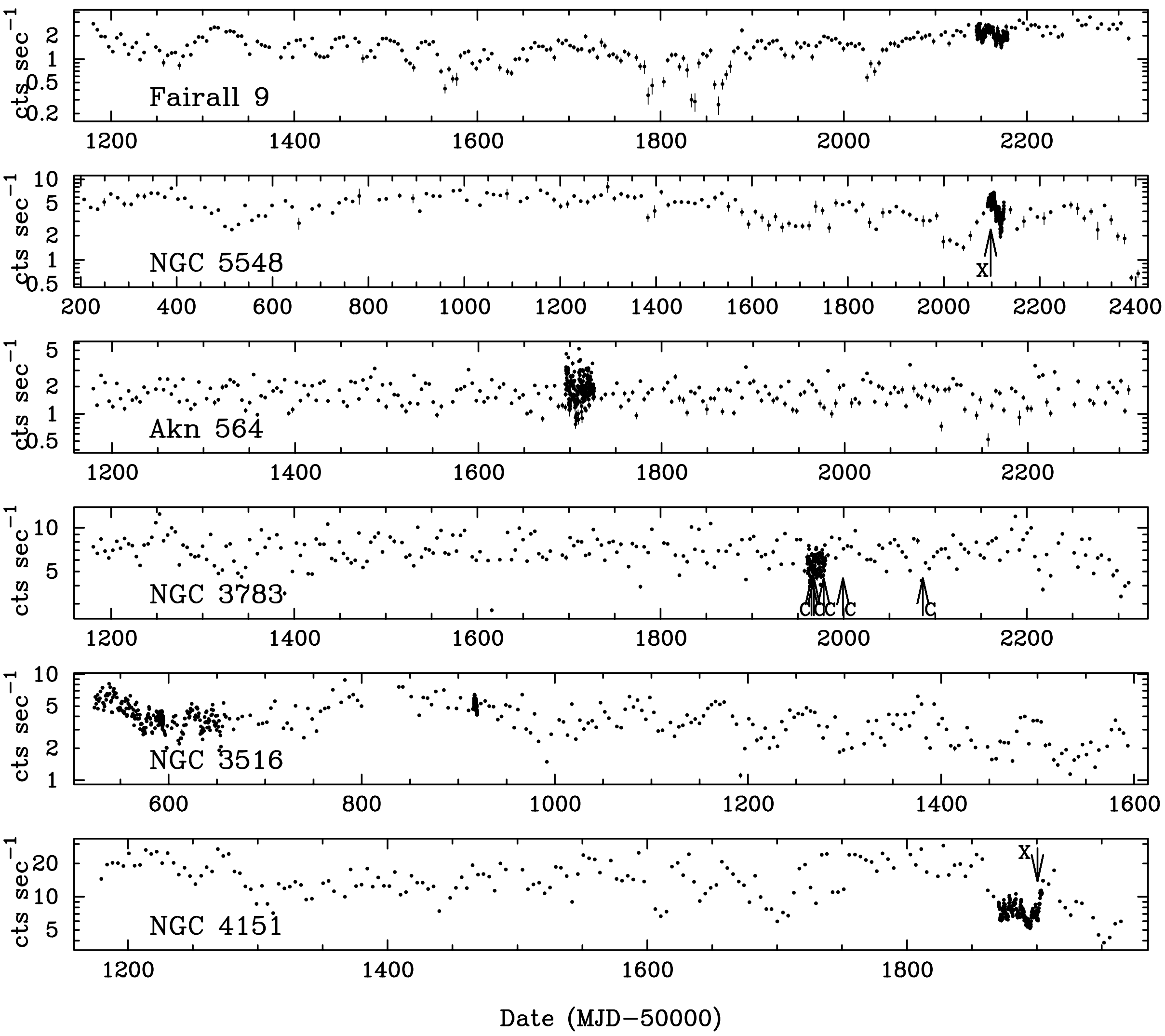

FIG. 1.—Plot of 2–10 keV *RXTE* "raw" light curves for the six targets. "X" and "C" denote location of *XMM-Newton* and *Chandra* long-looks, respectively. Count rates are all normalized to 1 PCU^{-1}.

Chandra long-looks marked. Figure 2 shows the long-term light curves resampled from the raw *RXTE* light curves. Figure 3 shows the resampled medium-term light curves, and Figure 4 shows the intensive long-looks. Table 2 summarizes the sampling parameters for each light curve, including the instrument, mean count rate, sampling interval, total points, and percent of missing data for each timescale for which there is even sampling suitable for PSD analysis. Also listed is $F_{\rm var}$, the square root of the excess variance, a measure of the intrinsic variability amplitude normalized to the mean as defined in, e.g., Edelson et al. (2002). We note that *RXTE*-PCA, *Chandra*-HETG, and *XMM-Newton* EPIC *pn* do not have precisely identical responses over the 2–10 keV bandpass; the PCA response is somewhat harder (peaking closer to ~5 keV) than that of the *pn* or *Chandra*-HETG (which peak closer to ~2 keV). It has been shown that the measured high-frequency PSD slope is energy dependent in both XRBs and Seyfert galaxies (Nowak et al. 1999a; Nandra & Papadakis 2001), flattening as photon energy increases; our use of *RXTE* data at low frequencies and *XMM-Newton* or *Chandra* at high frequencies could thus potentially mimic a high-frequency break. However, we expect this effect to be relatively minor because PSD slope typically flattens by only one- or two-tenths in power-law slope for a doubling or tripling of photon energy (Nowak et al. 1999a; Nandra & Papadakis 2001), and XRB and Seyfert PSD breaks typically involve a change in power-law slope near 1.

3. PSD CONSTRUCTION

The PSD construction required several steps. First, PSDs were measured for each individual short-, medium-, or long-timescale light curve, and then the individual PSDs were combined to form one high dynamic range PSD for each target, as described in § 3.1. However, these combined PSDs have poorly determined errors (dominated by systematic effects such as aliasing and red-noise leak, as described in § 3.2). A Monte Carlo technique was employed to better estimate PSD fit parameters in the presence of these systematic errors and distortion effects, as described in § 3.3.

3.1. *Initial Measurement*

First, light curves were linearly interpolated for missing data points, although such gaps were relatively rare. Light curves were not interpolated to a strictly even grid, since

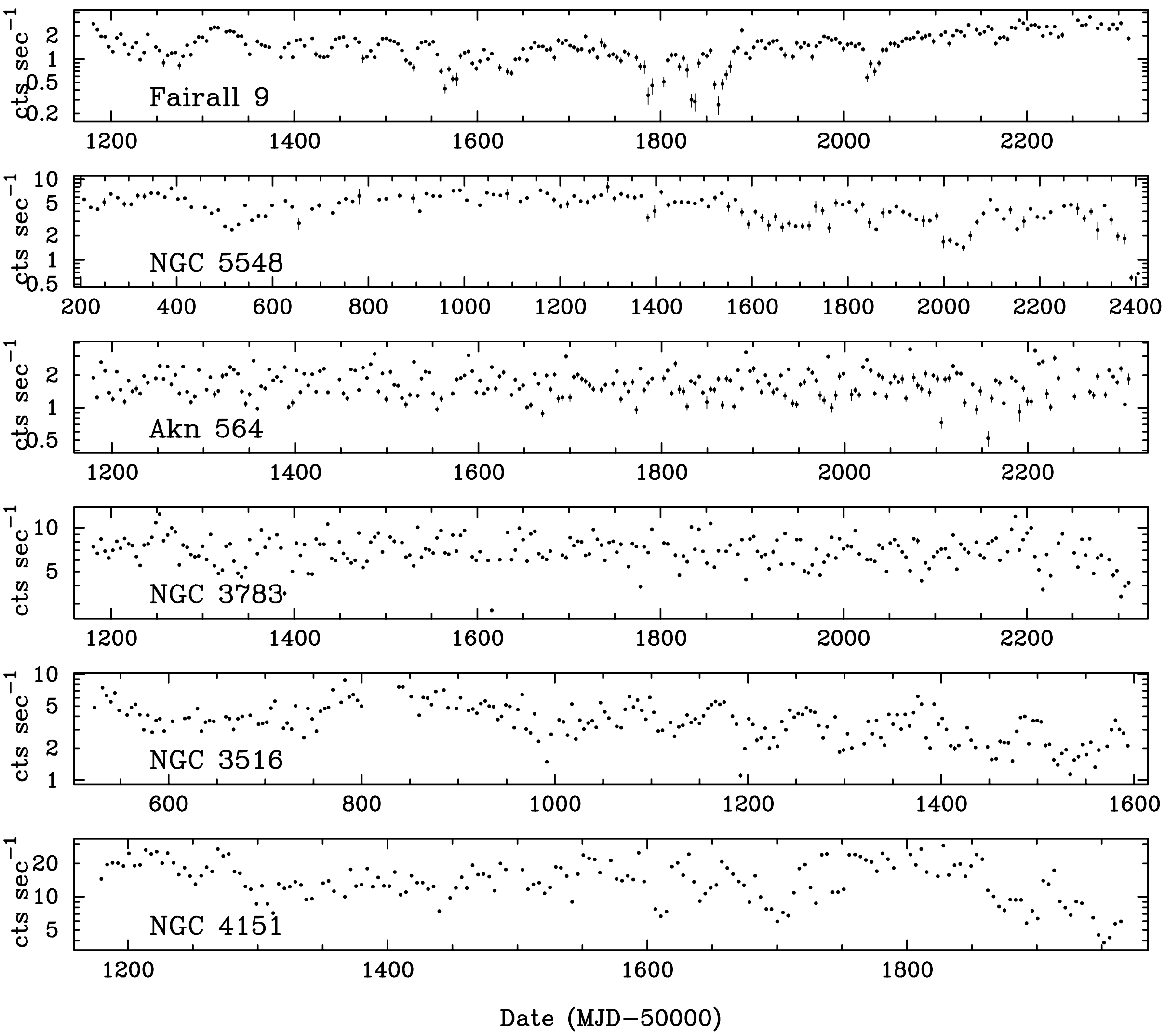

FIG. 2.—Plot of 2–10 keV *RXTE* long-term monitoring light curves for the six targets. Count rates are all normalized to 1 PCU^{-1}.

departures from ephemeris were almost always small (typically only a few percent) and such an interpolation would have negligible impact on the resulting periodogram. Each light curve's mean was subtracted.

The periodograms were constructed using a discrete Fourier transform (e.g., Oppenheim & Schafer 1975; Brillinger 1981). The power at each Fourier frequency $f = 1/D, 2/D, \ldots, 1/(2\Delta T)$ (the periodogram, where ΔT is the sampling time) was calculated using the fractional rms squared normalization

$$P(f) = \frac{2D}{\mu^2 N^2} |F(f)|^2 ,$$

where D is the duration, N is the number of points, μ is the mean count rate of the data, and $|F(f)|^2$ is the modulus squared of the Fourier transform of the light curve. The null, or rectangular, lag window was used; use of a tapered lag window for steep red-noise PSD data strongly increases the bias of the periodogram (see, e.g., Priestley 1981). Following Papadakis & Lawrence (1993a), the logarithm of the periodogram was binned every factor of 1.4 (0.15 in the logarithm) in temporal frequency, but the lowest frequency bins were widened to accommodate a minimum of two periodogram points. The constant level of power due to Poisson noise was not subtracted, but it was modeled in the Monte Carlo analysis. The individual PSDs were then combined to form broadband PSDs for each target.

These high-quality broadband PSDs spanned an exceptional range of timescales: four cover more than 4.4 decades of temporal frequency, and the other two cover 3.6 decades. PSD measurement parameters, including the minimum and Nyquist frequencies sampled in each PSD segment, are given in Table 3. No renormalization in power amplitude of the individual PSDs was done. The resulting broadband PSDs are shown in Figure 5. Visual inspection reveals a variety of behavior; e.g., low-frequency flattening is readily evident in the PSDs of NGC 3783 and Ark 564.

3.2. *Aliasing and Red-Noise Leak*

Although temporal analysis techniques such as the PSD are derived assuming continuous observations of infinite duration, such conditions cannot be attained in practice. These real-life Seyfert 1 sampling patterns $S(t)$ span a limited duration D and have a shortest time resolution $\Delta T_{\rm samp}$. Because the Fourier transform of the observed data is a convolution of the Fourier transform of the underlying

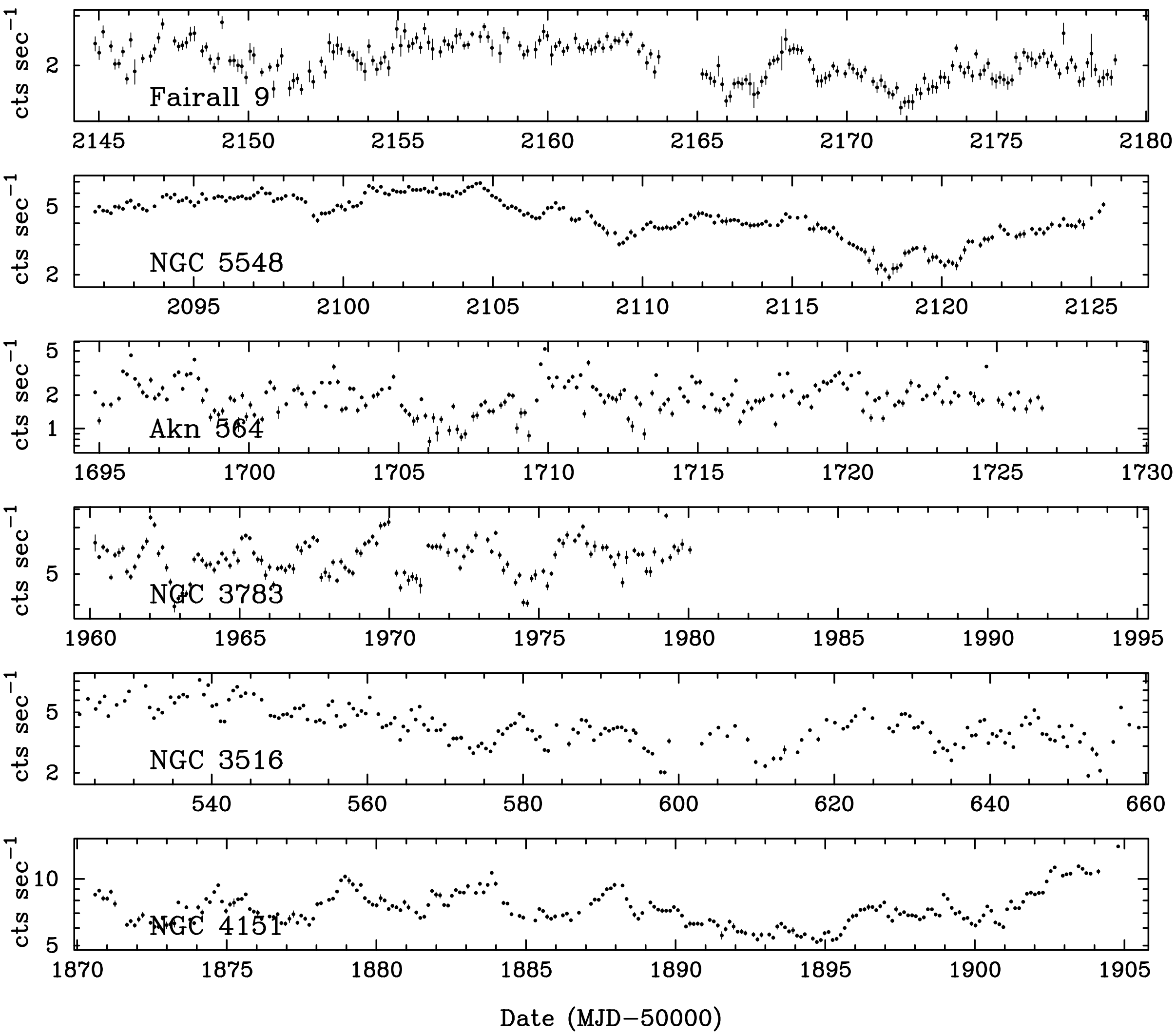

FIG. 3.—Plot of 2–10 keV *RXTE* medium-term monitoring light curves for the six targets. Count rates are all normalized to 1 PCU^{-1}.

variability process with $\hat{S}(f)$, the "sampling window," power is transferred into the sampled frequency range from above $f_{\rm Nyq} = 1/(2\Delta T_{\rm samp})$ and below $1/D$ (red-noise leak), as explained below.

If a red-noise PSD contains significant power below $f_{\rm min} = 1/D$, then there may be significant long-term trends present in the light curve. These trends can dominate the total variance of the observed light curve, whose measured PSD then contains additional power transferred from below $f_{\rm min}$. The power transferred by this red-noise leak process has a power-law slope that goes as f^{-2} (see details in van der Klis 1997).

On short timescales, the discrete sampling causes aliasing. For bins of width $\Delta T_{\rm bin}$ evenly spaced $\Delta T_{\rm samp}$ apart (with $\Delta T_{\rm bin} \ll \Delta T_{\rm samp}$), variations on timescales shorter than $\Delta T_{\rm samp}$ cannot be distinguished from longer timescale variations, and power from above $f_{\rm Nyq}$ is effectively added into the frequency range sampled by the PSD.

Distortion effects are present in, and hamper the interpretation of, the PSDs constructed above, but another serious problem with these PSDs is that the lowest temporal frequency bins contain too few PSD points for normal errors to be assigned. Binning a sufficient number of periodogram estimates ($\gtrsim 20$ for logarithmically binned periodograms; Papadakis & Lawrence 1993a) ensures that the averaged power will approach a Gaussian distribution, and the mean of the periodogram points in a frequency bin will tend to the power amplitude of the true underlying variability process, $P_{\rm true}(f)$.

3.3. *Monte Carlo Simulations*

To obtain a PSD shape with adequate errors, and to solve the problem of distortion effects, we use a version of Monte Carlo technique PSRESP first introduced by UMP02, based on a similar Monte Carlo technique by Done et al. (1992). This enables us to quantify the degree of low-frequency flattening and find a best-fit model PSD shape corresponding to the underlying variability process.

The technique consists of simulating light curves from a given PSD model shape specified for testing, resampling these light curves, and measuring their PSDs in the same manner as the observed light curves, forming an "average model" broadband PSD that accounts for the distortion effects. Errors are assigned for all frequency bins, derived from the rms spread of the individual simulated PSDs at a

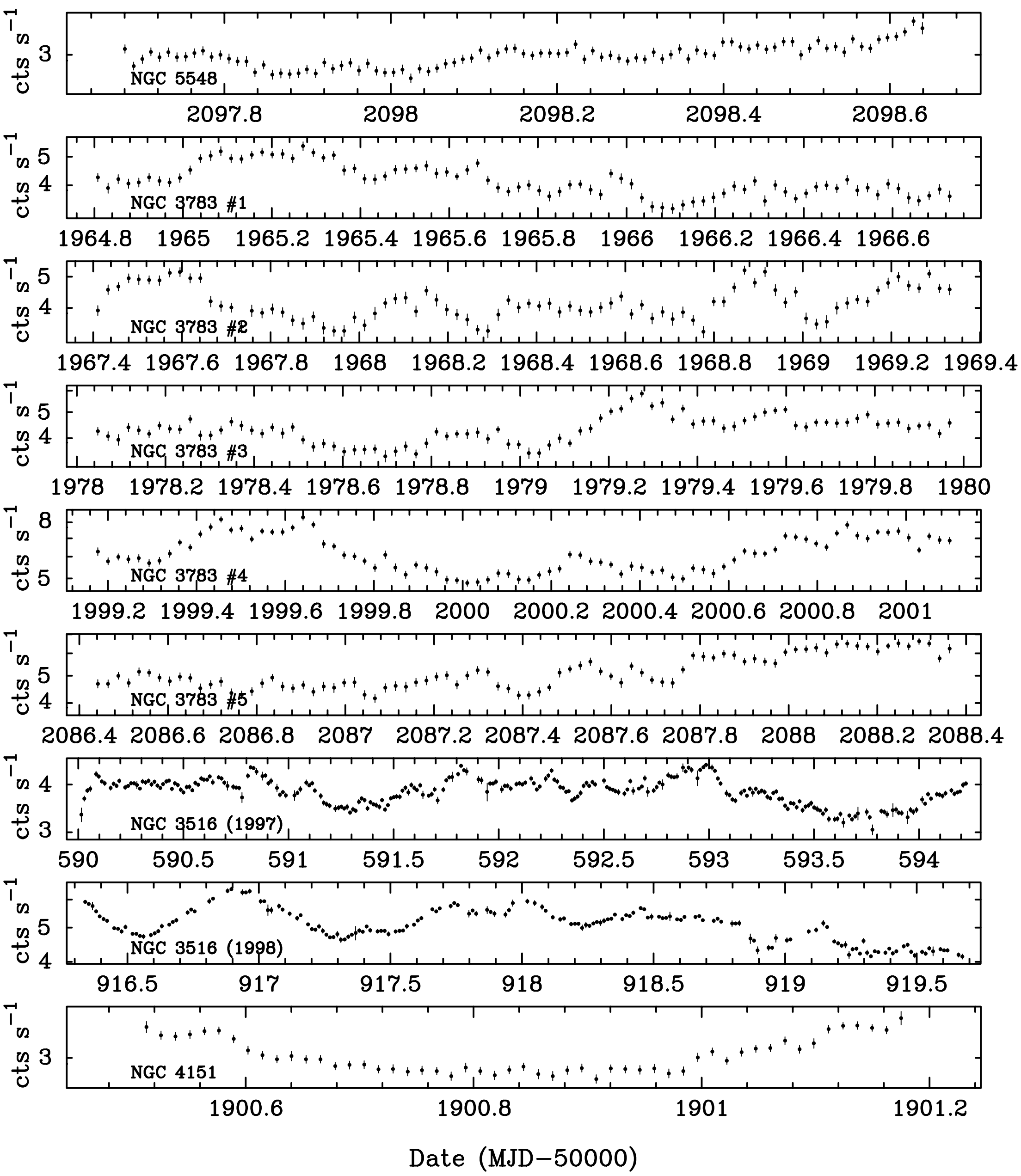

FIG. 4.—Plot of 2–10 keV continuous long-look light curves. *Top to bottom:* NGC 5548 with *XMM-Newton*, the five *Chandra* long-looks for NGC 3783, the 1997 and 1998 *RXTE* long-looks for NGC 3516, and NGC 4151 with *XMM-Newton*. Count rates have not been renormalized relative to each other. PCA count rates are all normalized to 1 PCU^{-1}.

given frequency bin. Finally, the technique compares the model broadband PSD to that derived from the observed data using a fit statistic with the distribution estimated from the simulations to determine goodness of fit for the model. In this manner, a variety of underlying PSD model shapes can be tested against the data. We note, as a caveat, that the results of this technique are highly model dependent; specifically, the primary assumption governing this entire process is that the broadband PSD model shape used for testing is an accurate representation of the underlying variability process $P_{\rm true}(f)$. An outline of the Monte Carlo method is as follows (see UMP02 for further details):

1. An underlying model PSD shape (a continuous function) is specified for testing. The initial normalization is arbitrary. For each long-, medium-, and short-term PSD segment, the algorithm of Timmer & König (1995) is used to generate N light curves (where N is at least 100). The time resolution $\Delta T_{\rm sim}$ is chosen to be $0.1\Delta T_{\rm samp}$. To ensure that the light curves account for variability on timescales longer than the observed light curve (contain a red-noise leak contribution if necessary), one very long segment of length ND is simulated; this is then broken up into N light curves, each of duration D.

2. The light curves are resampled in the same manner as the observed light curves as follows. For long- and medium-term simulated data, every tenth point is selected to degrade the resolution from $\Delta T_{\rm sim} = 0.1\Delta T_{\rm samp}$ to $\Delta T_{\rm samp}$; this correctly accounts for most of the total aliasing, specifically that portion of the aliased power that is due to variations on

TABLE 3

PSD Measurement Parameters

Source Name	Temporal Frequency Range Spanned (decades)	Timescale	$f_{\rm min}$ (Hz)	$f_{\rm Nyq}$ (Hz)	$P_{\rm Psn}$ ($\rm Hz^{-1}$)
Frl 9	3.6	Long	1.0×10^{-8}	1.4×10^{-6}	1360
		Medium	3.4×10^{-7}	4.4×10^{-5}	30.9
NGC 5548	5.0	Long	5.2×10^{-9}	1.4×10^{-6}	577
		Medium	3.4×10^{-7}	4.4×10^{-5}	9.4
		Short	1.2×10^{-5}	5.6×10^{-4}	0.69
Ark 564	3.6	Long	1.0×10^{-8}	1.4×10^{-6}	1050
		Medium	3.7×10^{-7}	4.4×10^{-5}	33.8
NGC 3783	4.4	Long	1.0×10^{-8}	1.4×10^{-6}	1210
		Medium	5.8×10^{-7}	4.4×10^{-5}	6.87
		Short	5.9×10^{-6}	2.5×10^{-4}	5.12
		Short	5.9×10^{-6}	2.5×10^{-4}	5.14
		Short	5.9×10^{-6}	2.5×10^{-4}	4.94
		Short	5.9×10^{-6}	2.5×10^{-4}	3.45
		Short	5.9×10^{-6}	2.5×10^{-4}	4.13
NGC 3516	4.6	Long	1.1×10^{-8}	1.4×10^{-6}	177
		Medium	8.5×10^{-8}	1.1×10^{-5}	13.8
		Short	2.8×10^{-6}	4.2×10^{-4}	0.37
		Short	3.5×10^{-6}	4.2×10^{-4}	0.23
NGC 4151	4.6	Long	1.1×10^{-8}	1.4×10^{-6}	44.2
		Medium	3.4×10^{-7}	4.4×10^{-5}	4.7
		Short	1.2×10^{-5}	4.5×10^{-4}	0.67

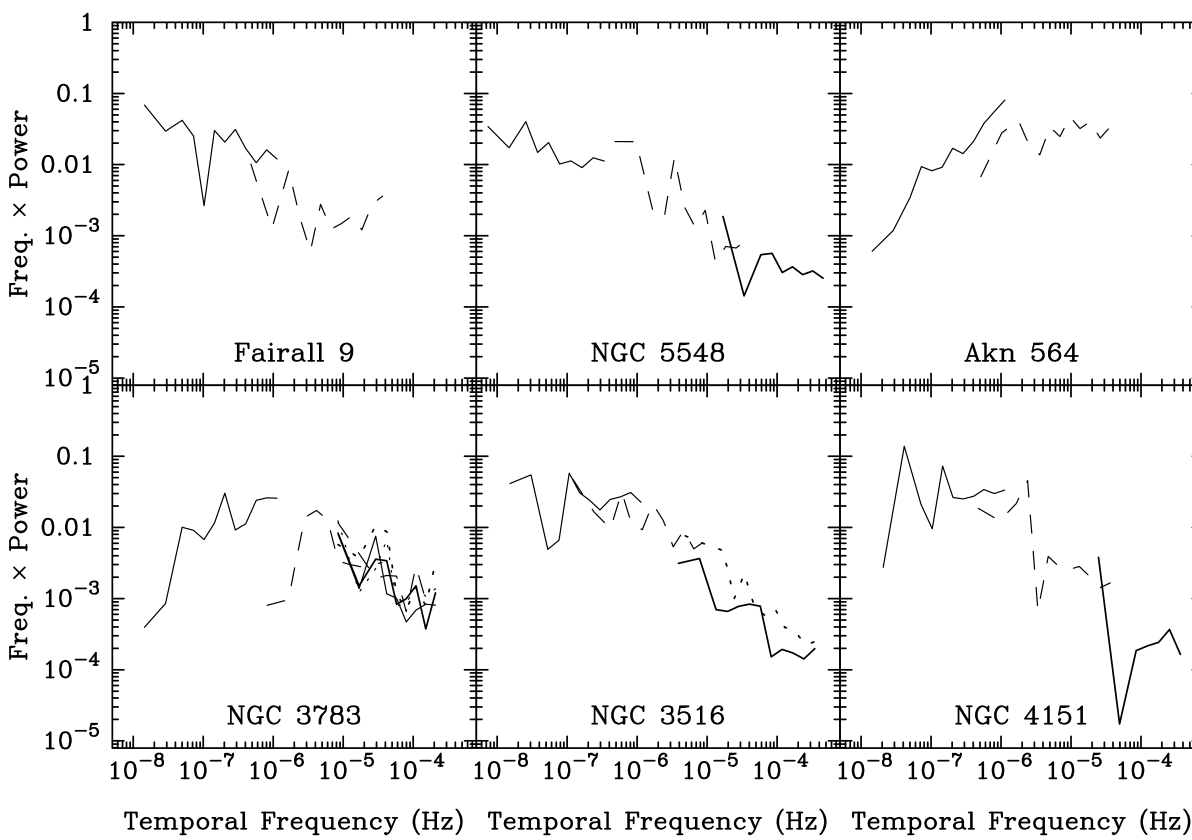

Fig. 5.—Raw broadband PSDs for the six targets, plotted in $f \times P_f$ space (units are Hz × $\rm Hz^{-1}$, or dimensionless). Such $f \times P_f$ plots are common in XRB PSD analysis; e.g., Sunyaev & Revnivtsev (2000). Targets are ranked by 2–10 keV luminosity; the power due to Poisson noise has not been subtracted from these PSDs. Each long-term PSD is marked by a solid line and each medium-term PSD by a dashed line. The short-term NGC 5548 and NGC 4151 PSDs are marked with a solid line. The NGC 3516 1997 and 1998 short-term PSDs are marked with solid and dotted lines, respectively. The NGC 3783 short-term *Chandra* PSDs, from first to last observed, are denoted by heavy solid, heavy dotted, solid, dashed, and dotted lines, respectively.

timescales from $f_{\rm Nyq}$ to $1/(2\Delta T_{\rm sim})$. For continuous long-look simulated data, the data are averaged over every 10 points. The uncertainty in the quantity of aliased power in red-noise PSD is dominated by the uncertainty in the amount of power at frequencies just above $f_{\rm Nyq}$, which is why this resampling procedure must be used. Time bins with missing flux in the observed light curves are linearly interpolated.

3. PSDs are constructed from the simulated light curves in the same manner as the observed PSDs, using the same normalization and frequency binning. For each segment, the model average PSD $\overline{P_{\rm sim}(f)}$ is calculated from the N individual PSDs; error bars $\Delta\overline{P_{\rm sim}(f)}$ equal to the rms spread of the individual PSDs at each frequency bin are assigned.

4. While the resampling approach in step 2 accounts for much of the total aliasing in red-noise PSDs, there remains aliasing due to variations on timescales from $\Delta T_{\rm sim}$ down to $\Delta T_{\rm bin}$. This second, smaller quantity of aliased power is approximated by adding a constant level of power to all frequencies sampled in a given PSD. Since variations on timescales shorter than $\sim 2\Delta T_{\rm bin}$ will likely not contribute to aliasing, this quantity of aliased power can be approximated by the analytical expression

$$P_{\rm alias} = \frac{1}{f_{\rm Nyq} - f_{\rm min}} \int_{(2\Delta T_{\rm sim})^{-1}}^{(2\Delta T_{\rm bin})^{-1}} P(f) df$$

(e.g., see UMP02 § 3.3) and added to the model average PSD and the N individual PSDs. The resulting PSDs then account fully for both red-noise leak and both aliasing components.

5. The goodness of fit is determined. Comparison of a model-average PSD to the observed PSD is not possible in the "traditional" χ^2 sense, since, as previously discussed, error bars assigned to the observed PSD are not strictly Gaussian. Instead, a new statistic $\chi^2_{\rm dist}$ is defined to compare the average distorted model PSD to the observed data, using the well-determined errors from the model:

$$\chi^2_{\rm dist} = \sum_f \frac{\left[\overline{P_{\rm sim}(f)} - P_{\rm obs}(f)\right]^2}{\left[\Delta\overline{P_{\rm sim}(f)}\right]^2} .$$

The total $\chi^2_{\rm dist}$ value is calculated by summing over all frequency bins in all PSD segments. For the targets with multiple short-term PSDs (NGC 3516 and NGC 3783), we average the values of short-term $\chi^2_{\rm dist}$ to avoid unnecessarily weighting the fit toward the highest frequencies.

The best-fitting normalization of the $P_{\rm sim}(f)$ is found by renormalizing all segments of the $P_{\rm sim}(f)$ by the same factor until the total $\chi^2_{\rm dist}$ value is minimized. The power contribution from Poisson noise is added to the model PSDs during this step; $P_{\rm Psn}$ is calculated via $2(\mu + B)/\mu^2$, where μ and B are the total source and background count rates, respectively. For noncontinuously observed light curves, this must be multiplied by $\Delta T_{\rm samp}/\Delta T_{\rm bin}$. The observed $\chi^2_{\rm dist}$ value is calculated.

The goodness of fit is then determined as follows: 10,000 combinations of the long-, medium-, and short-term simulated PSDs are randomly selected to model the $\chi^2_{\rm dist}$ distribution for each given PSD model. For each combination, the value of simulated $\chi^2_{\rm dist}$ [comparing $P_{\rm sim}(f)$ to $\overline{P_{\rm sim}(f)}$] is calculated. These 10,000 measurements of the simulated $\chi^2_{\rm dist}$ distribution are sorted into ascending order. The probability that the model PSD can be rejected is given by the percentile of the 10,000 $\chi^2_{\rm dist}$ exceeded by the value of observed $\chi^2_{\rm dist}$.

6. The above steps are repeated to test a range of PSD model shapes by stepping through a range of high-frequency slopes and break frequencies.

4. RESULTS

The results of the Monte Carlo analysis are presented for several simple PSD model shapes to quantify the degree of flattening, if any, toward low temporal frequencies. First, unbroken PSD models are tested (§ 4.1). Then, models incorporating a single PSD break are tested (§ 4.2). We do not test for quasi-periodic oscillations (QPOs); although they are routinely seen in XRB PSDs, there is no obvious indication of QPOs in the observed light curves or resultant PSDs, and there has been no convincing evidence to date for deterministic behavior in AGN light curves or PSDs (e.g., Lawrence et al. 1987; McHardy & Czerny 1987) because previous claims of QPOs in AGNs (e.g., Papadakis & Lawrence 1993b) all either have been refuted or lack confirmation. Preliminary evidence for a doubly broken power-law model fit to the PSD of NGC 3783 is presented in § 4.3. Finally, a test of one of the assumptions governing the PSD construction, the assumption of PSD stationarity, is presented in § 4.4.

4.1. *Unbroken Power-Law Models*

The simplest model tested was an unbroken power law, of the form $P(f) = A_0(f/f_0)^{-\beta}$, where the normalization A_0 is the PSD amplitude at $f = f_0$ and β is the power-law slope. (The constant level of power from Poisson noise is added to each simulated PSD, but because this value is different for each long-, medium-, and short-term PSD segment, it is not explicitly listed here.) For all targets, the model was tested by stepping through the range of β from 1.0 to 4.0 in increments of 0.05; for Ark 564 and NGC 3783, the two targets with relatively flatter observed PSDs, values of β down to 0.0 were additionally tested. Five hundred simulated PSDs were used to determine the average model PSD, and 10^4 randomly selected sets of PSDs were used to probe the simulated $\chi^2_{\rm dist}$ distribution.

The best-fitting models and simulated data are plotted in $f \times P_f$ space in Figure 6 for all targets. The best-fitting values of β and A_0, along with the corresponding likelihood of acceptance (defined as $1 - R$, where R is the rejection confidence), are summarized in Table 4. The errors on β correspond to values 1 σ above the likelihood of acceptance for the best-fit value on a Gaussian probability distribution (i.e., the amount β needs to change for the fit to be less likely by 1 σ). While we have not yet rigorously proven the validity of these errors, this method does give very reasonable values. The errors on A_0 are determined from the rms spread of the 10^4 randomly selected sets of simulated PSDs. The low likelihood of acceptance for NGC 3783, for instance, indicates that an unbroken power law is an inaccurate description of the data.

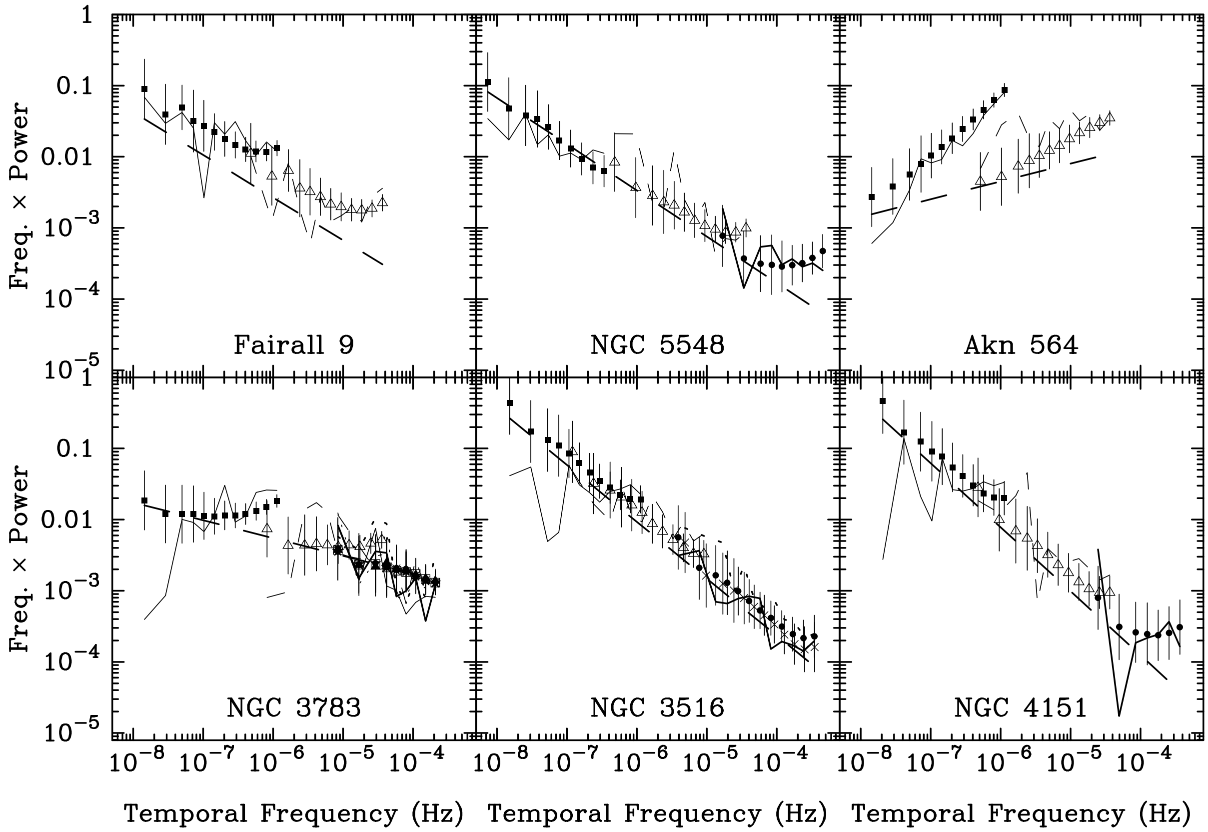

FIG. 6.—Comparison of the best-fitting unbroken power-law model against the observed PSDs, plotted in $f \times P_f$ space. The observed PSD points are denoted by solid, dashed, or dotted lines as described in Fig. 5. The best-fitting average distorted PSD model is denoted by symbols as follows: filled squares denote PSD derived from long-term monitoring; open triangles, medium-term monitoring; filled circles, the short-term monitoring for NGC 5548, NGC 4151, and the 1997 long-look of NGC 3516; crosses, the 1998 long-look of NGC 3516. The five NGC 3783 *Chandra* PSDs, from first to fifth, are marked by filled circles, crosses, open squares, filled stars, and filled triangles. The heavy dashed line represents the best-fitting unfolded PSD model shape, excluding the distortion effects and Poisson noise, which are evident in the observed and simulated PSD points. Note, for instance, the large quantity of aliasing present in the long-term PSD segment of Ark 564 because of the very high levels of short-term variability in that object.

4.2. *Singly Broken Power-Law Models*

To test for the presence of a PSD break, we employed a broken power-law model of the form

$$P(f) = \begin{cases} A(f/f_c)^{-\gamma}\ , & f \le f_c\ , \\ A(f/f_c)^{-\beta}\ , & f > f_c\ , \end{cases}$$

TABLE 4

RESULTS FOR UNBROKEN POWER LAW MODEL FIT

Target	Best-fitting β	Best-fitting A_0 (Hz^{-1})	Likelihood of Acceptance (%)
Frl 9	$1.60^{+2.40}_{-0.20}$	$(2.7 \pm 0.4) \times 10^3$	11.3
NGC 5548.......	$1.65^{+0.20}_{-0.10}$	$3.4^{+0.6}_{-0.5} \times 10^3$	37.2
Ark 564...........	$0.75^{+0.40}_{-0.10}$	$(4.5 \pm 0.5) \times 10^3$	0.6
NGC 3783.......	1.25	$(5.5 \pm 0.5) \times 10^3$	<0.01
NGC 3516.......	$1.80^{+2.20}_{-0.35}$	$9.3^{+1.6}_{-1.9} \times 10^3$	6.6
NGC 4151.......	$1.90^{+2.10}_{-0.35}$	$7.8^{+3.4}_{-2.4} \times 10^3$	1.8

NOTE.—Results from fitting the PSDs with an unbroken power law model. The quantity A_0 is the power amplitude at $f = 10^{-6}$ Hz. The likelihood of acceptance is defined as $(1 - R)$, where R is the rejection confidence. No error is assigned for the best-fitting β for NGC 3783. Upper limits on β for Frl 9, NGC 3516, and NGC 4151 cannot be constrained because of a red-noise leak bias discussed in the text.

where the normalization A is the PSD amplitude at the break frequency f_c, β is the high-frequency power-law slope, and γ is the low-frequency power-law slope, with the constraint $\gamma < \beta$. The range of slopes tested was $\beta = 0.0$–4.0 in increments of 0.05. Break frequencies were tested in the log from -8.0 to -4.0 in increments of 0.1, corresponding to $f \rightarrow 1.26f$ in the linear scale. One hundred simulated PSDs were used to determine the average model PSD, and 10^4 randomly selected sets of PSDs were used to probe the χ^2_{dist} distribution.

Figure 7 shows the best-fitting singly broken PSD model shape and simulated data for each target, plotted in $f \times P_f$ space. Figure 8 shows contour plots for the best-fitting singly broken model fixed at the best-fitting value of γ. The presence of a constant Poisson power level dominates the steepest PSD slopes and leads to degeneracy in that most values of β above ~ 3 can lead to the same rejection probability (e.g., upper limits on β for NGC 4151 cannot be constrained); a relatively more minor effect is that excessive red-noise leak from very steep PSD slopes ($\beta \gtrsim 2.5$) increases the errors, with the result that excessively large errors decrease the reliability of the values of the rejection probability. For each target, the best-fitting values of β, γ, f_c, and A and the likelihood of acceptance are summarized in Table 5. As before, errors on a single parameter are 1 σ above the likelihood of acceptance for the best-fit value. The reader

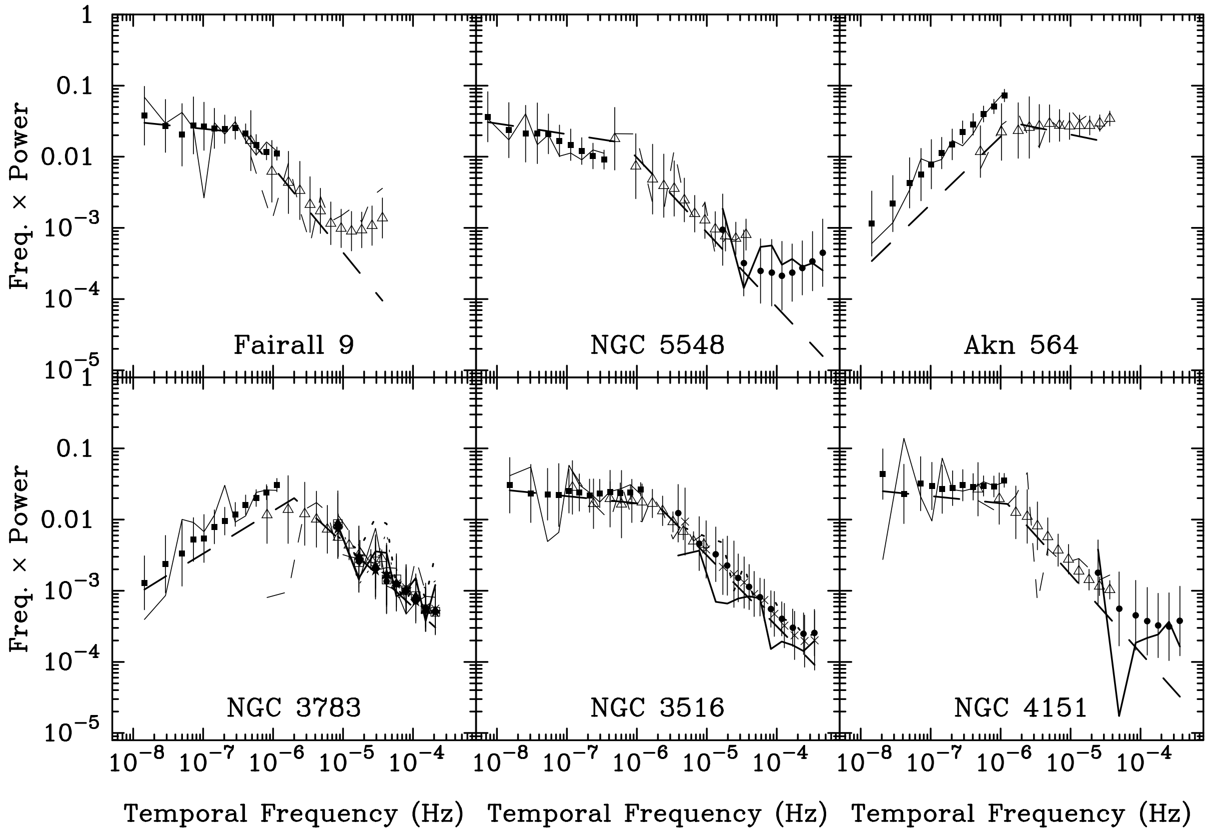

FIG. 7.—Comparison of the best-fitting singly broken power-law model fits against the observed PSDs, plotted in $f \times P_f$ space. All lines and symbols are the same as in Fig. 6.

can also refer to the contour plots of Figure 8 for estimates of the absolute rejection probabilities for a given set of parameters. For Ark 564, no lower limit to γ is given; models with blue-noise ($\gamma < 0$) PSD components are dominated by the aliased power, resulting in degenerate values of the rejection probability for any $\gamma < 0$. The errors on A are determined from the rms spread of the 10^4 randomly selected sets of simulated PSDs.

For all six sources, the likelihood of acceptance improves when the break is added to the fit, as illustrated by the values of $\Delta\sigma$, the increase in likelihood of acceptance between the unbroken and singly broken power-law fits, listed in column (7) of Table 5. This in itself indicates problems with the pure power-law model. In four PSDs (Ark 564, NGC 3783, NGC 3516, and NGC 4151), the unbroken power-law fit is accepted at less than 10% confidence while the singly broken power law is accepted at greater than 10% confidence. (That is, the rejection probability drops from greater than to less than 90%). These are significant improvements, corresponding to an increase in likelihood of acceptance of 0.9–2.9 σ for these four sources. In the remaining two cases (Frl 9 and NGC 5548) unbroken power-law fits were already reasonably acceptable (11.3% and 37.2% likelihood of acceptance) so the addition of a break improves the likelihood of acceptance by only 0.4–0.6 σ.

TABLE 5

RESULTS FOR SINGLY BROKEN POWER LAW MODEL FITS

Target	γ	β	f_c (Hz)	A (Hz^{-1})	Likelihood of Acceptance (%)	$\Delta\sigma$
Frl 9	$1.10^{+1.10}_{-0.60}$	$2.20^{+0.65}_{-0.20}$	$3.98^{+2.33}_{-2.40} \times 10^{-7}$	$5.4^{+0.8}_{-0.7} \times 10^4$	23.5	0.6
NGC 5548	$1.15^{+0.50}_{-0.65}$	$2.05^{+0.80}_{-0.40}$	$6.31^{+18.8}_{-5.05} \times 10^{-7}$	$2.5^{+0.5}_{-0.4} \times 10^4$	87.4	0.4
Ark 564	$0.05^{+0.55}_{-2.05}$	$1.20^{+0.25}_{-0.35}$	$1.59^{+4.73}_{-0.95} \times 10^{-6}$	$1.9^{+0.1}_{-0.2} \times 10^4$	97.3	2.9
NGC 3783	$0.40^{+0.25}_{-0.35}$	$1.90^{+0.15}_{-0.30}$	$2.00^{+3.01}_{-0.74} \times 10^{-6}$	$(1.0 \pm 0.1) \times 10^4$	12.7	2.0
NGC 3516	$1.10^{+0.40}_{-0.30}$	$2.00^{+0.55}_{-0.20}$	$2.00^{+3.01}_{-1.00} \times 10^{-6}$	$7.9^{+0.8}_{-0.7} \times 10^3$	81.1	1.9
NGC 4151	$1.10^{+1.35}_{-0.40}$	$2.10^{+1.90}_{-0.25}$	$1.26^{+1.90}_{-1.01} \times 10^{-6}$	$(1.3 \pm 0.2) \times 10^4$	10.8	0.9

NOTE.—Results from fitting the PSDs with the singly broken power law model. The quantity γ is the low-frequency power-law slope, β is the high-frequency power-law slope, and A is the power amplitude at the break frequency f_c. The likelihood of acceptance is again defined as $(1 - R)$, where R is the rejection confidence. The $\Delta\sigma$ quantifies the increase in likelihood of acceptance between the unbroken and singly broken power law fits.

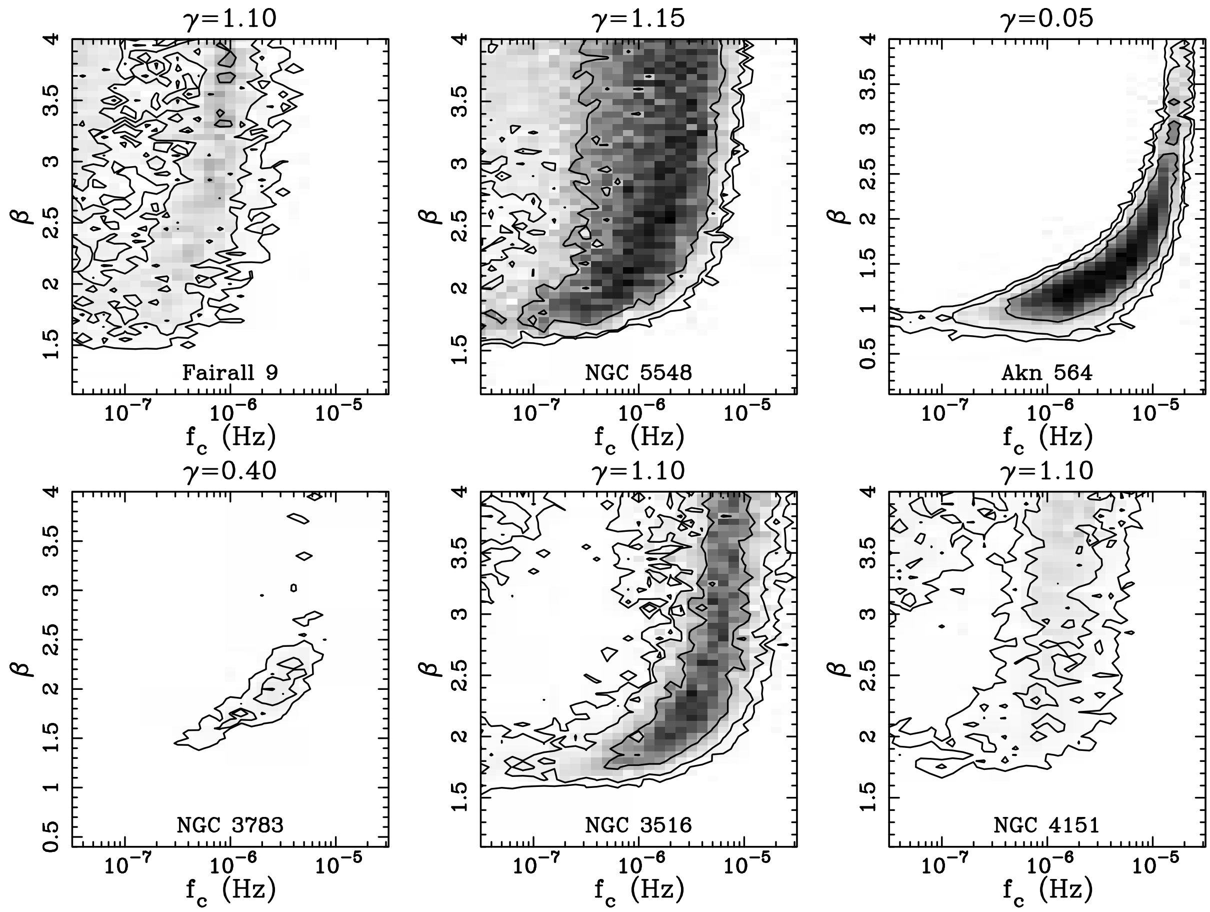

Fig. 8.—Contour plots showing the errors on the best-fitting singly broken PSD model shape. For each target, a slice through the three-dimensional fit parameter space at the best-fitting low-frequency slope is shown. Solid lines indicate the 99%, 95%, and 68% rejection probability levels. Lighter shading denotes a high rejection probability; darker shading denotes a low rejection probability.

4.3. *A Doubly Broken Power Law in NGC 3783?*

Inspection of Figure 7 suggests that the PSD NGC 3783 is steep at high frequencies, then flattens out in $f \times P_f$ space (a slope of ≈ -1 in P_f space), then turns downward in $f \times P_f$ space (to a slope of ≈ 0 in P_f space) at the lowest frequencies probed. This behavior is reminiscent of low-state XRBs (e.g., Nowak et al. 1999a) and suggests an improvement upon the singly broken fit in NGC 3783.

In order to test for a second break, we employ a model of the form

$$P(f) = \begin{cases} A_l\,, & f \le f_l\,, \\ A_h(f/f_h)^{-1}\,, & f_l < f \le f_h\,, \\ A_h(f/f_h)^{-\beta}\,, & f > f_h\,, \end{cases}$$

where A_l is the PSD amplitude below the low-frequency break f_l, where the PSD has zero slope. The intermediate slope, between the two break frequencies, is fixed at -1 in order to fix this model with the same number of free parameters as the singly broken model. The quantity $A_h = A_l(f_h/f_l)^{-1}$ and equals the PSD amplitude at the high-frequency break f_h; the PSD slope above f_h is $-\beta$. Break frequencies were tested in the log from -8.0 to -4.0 in increments of 0.1, corresponding to $f \rightarrow 1.26f$ in the linear scale. The range of β tested was 1.1–2.4 in increments of 0.1. One hundred simulated PSDs were used to determine the average model PSD, and 10^4 randomly selected sets of PSDs were used to probe the $\chi^2_{\rm dist}$ distribution.

The best-fitting model, plotted in Figure 9, has a low-frequency break at $f_l = 2.00^{+3.01}_{-1.20} \times 10^{-7}$ Hz, a

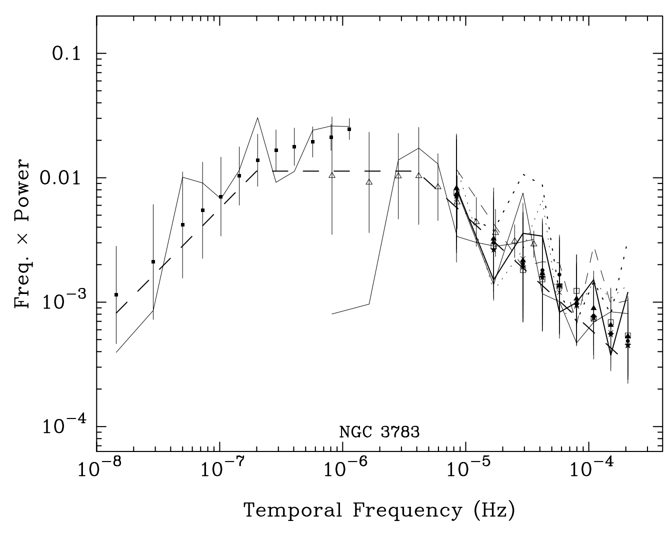

Fig. 9.—Comparison of the best-fitting doubly broken power-law model fit to the observed NGC 3783 PSD, plotted in $f \times P_f$ space. All lines and symbols are the same as in Fig. 6.

high-frequency break at $f_h = 3.98^{+6.02}_{-1.47} \times 10^{-6}$ Hz, and a power-law slope of $\beta = 2.0 \pm 0.3$ in P_f space above the high-frequency break. The best-fitting power amplitudes are $A_h = 2.8^{+0.3}_{-0.2} \times 10^3$ Hz^{-1} and $A_l = 5.6^{+0.6}_{-0.5} \times 10^4$ Hz^{-1}. The likelihood of acceptance is 25.5% (rejection probability of 74.5%), only a modest improvement over the singly broken power-law model fit. The evidence in favor of two breaks in the NGC 3783 PSD is therefore only tentative at this point.

One can speculate, however, that the value of $\gamma = 0.40^{+0.25}_{-0.35}$ in the best-fitting singly broken power-law model for NGC 3783 actually reflects an average of the intermediate and white-noise portions of a doubly broken PSD. More significantly, when γ in the singly broken model is fixed to the intermediate power-law slope of -1 (similar to the best-fit singly broken models for the other broad-line Seyfert 1 targets), the best fit, with $\beta = 1.95^{+0.15}_{-0.20}$ and $f_c = 6.31^{+3.89}_{-3.80} \times 10^{-6}$ Hz, has a very low likelihood of acceptance, 2.2% (rejection probability of 97.8%).

If Seyfert 1 PSDs do resemble XRB PSDs and have an intermediate power-law slope of -1, then the PSD of NGC 3783 does require a second break and resembles strongly the PSDs of low-state XRBs.

4.4. *Testing the Stationarity of the Light Curves*

In order to combine the different timescale PSDs to synthesize a single broadband PSD, we must assume that the specific short-timescale PSD measured in a single intensive *XMM-Newton* or *Chandra* observation is representative of the average short-timescale PSD that would have been measured if the source was monitored continuously for the entire $\sim$3 yr period. We have tested this assumption using the five *Chandra* scans of NGC 3783, all taken with identical sampling intervals and durations. Each was used to measure separate short-timescale PSDs, which have identical spectral coverage and suffer the same levels of red-noise leak and aliasing. This allows a straightforward comparison, as shown in Figure 10. Note that all the PSDs show identical slopes to within the errors, and the amplitude normalization varies by $\sim$40%. This small range of amplitudes is fully consistent with stationary behavior, providing support for a key assumption of the PSD synthesis technique, and consistent with the linear rms-flux relation in the light curves of XRBs and Seyfert 1 galaxies discussed in Uttley & McHardy (2001).

The assumption of nonstationarity in the PSD applies not only to the short-term data but must be applicable to the long-term light curves as well. To examine the assumption of stationarity on long timescales, we halved all the long-term light curves and applied the Monte Carlo analysis to the resulting PSDs by assuming the best-fitting model for each target. Reasonable fits were obtained for all targets, supporting stationarity of the PSDs on timescales of $\gtrsim$1.5 yr.

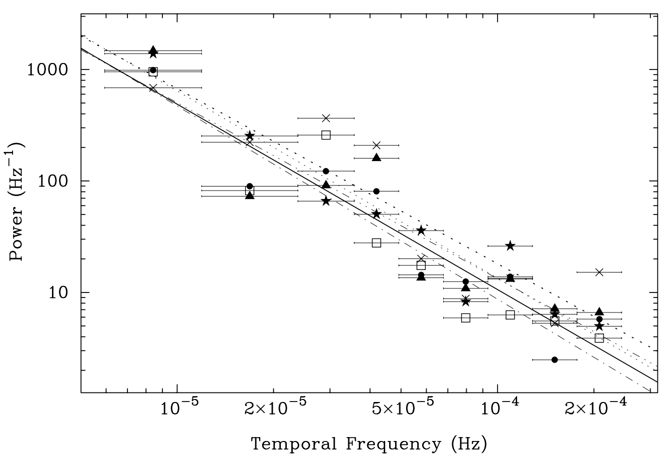

FIG. 10.—Five NGC 3783 *Chandra* short-term binned PSDs. From the first observed to last observed, the PSDs are marked by filled circles, crosses, open squares, filled stars, and filled triangles. The constant level of power due to Poisson noise has not been subtracted, although the Poisson noise levels are very similar for each observation. PSD errors are omitted here; they are determined later for a given PSD model shape. The best-fit lines (from first to last observed, represented by heavy solid, heavy dotted, solid, dashed, and dotted lines, respectively) were calculated assuming equal weighting to all points, but they are meant only to guide the eye and are not an accurate representation of the intrinsic, underlying PSD slope because of the presence of red-noise leak and power due to Poisson noise.

5. DISCUSSION

The fitting results are summarized in Figure 11, which allows the reader to directly assess the significance of features in the PSDs. These data are plotted in "model space" for ease of interpretation, with the data shifted relative to the model as required to account for aliasing and other distorting effects. This is the opposite of the earlier figures, done in "data space" in which the model is shifted to account for distortion effects.

The plot shows clearly the inadequacy of describing these PSDs as traditional red-noise pure power laws. All of the PSDs appear to show a similar departure from power-law behavior, a flattening to lower temporal frequencies, although the break strength and frequencies differ from object to object. The downturn is greatest in the PSDs of NGC 3783 (for which a "double break" is tentatively favored) and Ark 564. NGC 3516 and NGC 4151 also show strong breaks. This is confirmed by statistical tests, which find that addition of a break improves the likelihood of acceptance from less than 10% confidence to greater than 10% confidence for all four of these PSDs (see § 4.2.). On the other hand, the PSDs of NGC 5548 and Frl 9 are much steeper, with a turnover at lower temporal frequencies, and the addition of a break is not statistically significant. Only the upper limits to the break frequencies measured for Frl 9 and NGC 5548 will be considered henceforth. We conclude that there is clear visual and statistical evidence of a significant flattening in four of these objects and visual indications of a break in the remaining two. The implications of these results are discussed below.

5.1. *Comparison with Previous Results*

The present analysis finds a break in the PSD of NGC 3516 at a frequency of 2×10^{-6} Hz (corresponding to a timescale of 6 days), a factor of $\sim$5 higher frequency than the break found by EN99 in this object. The most likely cause for this discrepancy is the fact that EN99 forced the power-law slope below the break to zero; the present analysis finds a much steeper low-frequency slope, leading to the PSD break being modeled to occur at higher frequencies.

In their analysis of the Ark 564 PSD, Pounds et al. (2001) also forced the low-frequency slope to zero and also found a power-law slope above the break consistent with -1, consistent with the model fit in this work. However, the present

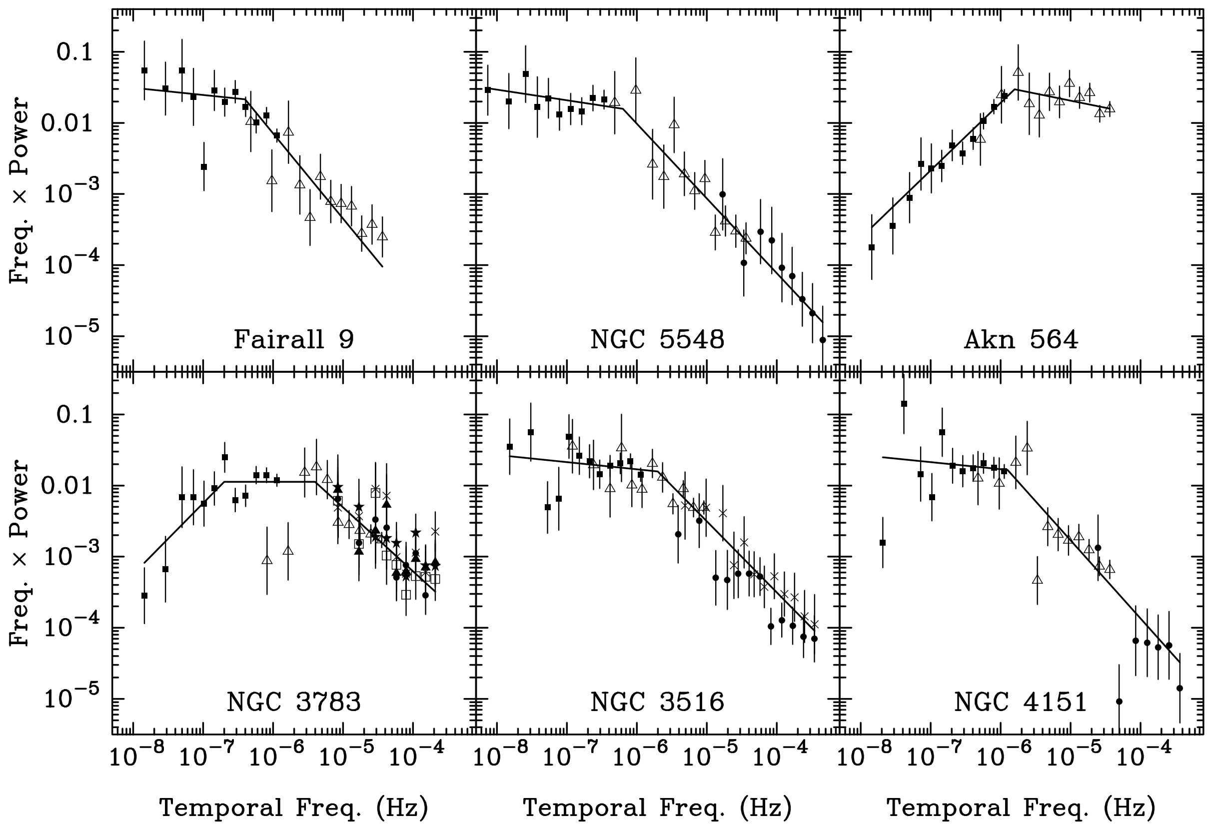

FIG. 11.—Best-fitting model fits (doubly broken power-law model for NGC 3783, singly broken power-law model for all other targets) are shown with the effects of Poisson noise, aliasing, and red-noise leak subtracted off. The solid line indicates the underlying, intrinsic PSD model shape. Symbols represent the differences between the average distorted model and the observed PSD data, plotted relative to the underlying PSD model shape.

work finds a break frequency that is a factor of ∼2 higher; this is most likely due to the fact that Pounds et al. (2001) did not account for the large quantity of aliased power present in the PSD and allowed the relative normalizations of individual PSD segments to vary.

The sample of four objects in UMP02 was chosen on the basis of known strong X-ray variability, whereas the current sample was chosen for 2–10 keV flux (Piccinotti et al. 1982). The UMP02 sample could hence be biased toward rapid variability. Two objects in the UMP02 sample, NGC 3516 and NGC 5548, overlap with ours, and the PSD analyses yield consistent results. The two other objects, NGC 5506 and MCG −6-30-15, are modeled to show very high frequency breaks ($\sim 5 \times 10^{-5}$ Hz) when a break to a fixed low-frequency slope of −1 is assumed; however, it also should be noted that fitting these objects' broadband PSDs with a model incorporating a fixed low-frequency slope of 0 yields PSD breaks located an order of magnitude lower in frequency. NGC 5506, from the UMP02 sample, is a Seyfert 2 and will not be discussed further. MCG −6-30-15 will be included along with the other six Seyfert 1 galaxies in the ensuing subsections below.

In their PSD analysis, Hayashida et al. (1998) defined a characteristic variability frequency in the PSDs of AGNs and Cyg X-1 as being the frequency at which the $f \times P_f$ power crossed a certain threshold value (10^{-3}). For the PSD shapes observed in XRBs and Seyfert galaxies, such a frequency is dependent on the PSD break frequency, high-frequency slope, and normalization. However, all these quantities can vary in XRBs, leading to degenerate values of the characteristic variability frequency for a given black hole mass. It is also more plausible that the break frequencies, and not the high-frequency slopes, are more closely connected to the black hole mass (see § 5.3). Furthermore, the distortion effects of red-noise leak and aliasing were not taken into account when those PSDs were determined.

Complementary to the work of Pounds et al. (2001), Papadakis et al. (2002) claim evidence for a break in PSD slope from ∼−1.3 to ∼−1.7 above a temporal frequency of $\sim 2 \times 10^{-3}$ Hz in Ark 564. However, Papadakis et al. (2002) estimate the high-frequency noise level simply from the average flux errors. Consequently, any small error in this noise level determination, which dominates the highest frequencies probed, requires a substantial change in high-frequency PSD slope. Additionally, that only *ASCA* data were used leaves about $\frac{2}{3}$ of an order of magnitude of temporal frequency uncovered because of Earth occultation gaps; more importantly, distortion effects are not considered.

5.2. *Comparison with X-Ray Binaries*

The Seyfert PSDs are much more poorly defined than those seen in low-state XRBs (e.g., Nowak et al. 1999a; Nowak, Wilms, & Dove 1999b). McHardy (1988) first made the link between the two types of compact systems based on similar slopes of the *EXOSAT* power-law PSDs (see also Lawrence & Papadakis 1993). The detection of Seyfert 1 PSD breaks (e.g., EN99), on timescales that appear to scale linearly with the breaks seen in XRBs, helped confirm this picture. Furthermore, the energy spectra of both types of objects are similar, featuring a nonthermal hard X-ray coronal power law that steepens as the source brightens (e.g., Markowitz & Edelson 2001; Wilms et al. 1999), a 6.4 keV Fe Kα fluorescence line modeled to originate in the regime of strong gravity (Tanaka et al. 1995; Fabian et al. 1995; Wilms et al. 1999), and a Compton reflection hump around 20–30 keV. These spectral components, along with the rapid X-ray variability and PSD similarities such as the energy dependence of the PSDs (Nandra & Papadakis 2001) and apparent phase lags (Papadakis, Nandra, & Kazanas 2001), support common X-ray emission and variability mechanisms in both classes of compact objects.

The observed PSD break frequencies in Seyfert galaxies are about 6–7 orders of magnitude smaller than those seen in low-state XRB PSDs. It is remarkable to note that this ratio is approximately the same as that of the X-ray luminosities and putative black hole masses (10 $M_\odot$ for Cyg X-1, Herrero et al. 1995; 10^7–10^8 $M_\odot$ for Seyfert galaxies, e.g., Kaspi et al. 2000). This scaling supports the picture of similar variability processes operating in both types of accreting compact systems. It is noted that this type of scaling is subject to the caveat of Seyfert galaxies and low-state XRBs differing *only* in mass, physical size, luminosity, and variability timescale. In fact, differences between the two classes of objects, most notably lower inner accretion disk temperatures in Seyfert galaxies than seen in low-state XRBs, prevent the analogy from being solidified.

However, key questions remain in this picture. Are the PSD shapes really identical between the two types of systems? The fact that XRB PSDs do not strictly adhere to a doubly broken power law (e.g., GX 339-4; Nowak et al. 1999b) and that our analysis only quantifies the overall broad PSD shape in terms of simple broken power laws hinders this issue. The sharpness of these models' breaks lacks a physical basis, but the data are not adequate to accurately constrain the "bluntness" of the break. Do the Seyfert PSD breaks seen correspond to the high- or low-frequency breaks seen in XRB PSDs? The tentative finding of two PSD breaks in NGC 3783 matches closely the double breaks in XRB PSDs, and the ratios of the break frequencies in both objects are nearly the same ($\sim$20 for NGC 3783, $\sim$20 for Cyg X-1 by Nowak et al. 1999a; 25 for the ratio of the average Cyg X-1 break frequencies; Belloni & Hasinger 1990), although the low-frequency break in Cyg X-1 is somewhat more variable, so these ratios should be taken with a grain of salt. For the other Seyfert galaxies, however, this issue is not as clear. The singly broken model fits for the PSDs of NGC 3516, NGC 4151, and to a lesser extent NGC 5548 and Frl 9 appear similar to the high-frequency break in XRBs in terms of incorporating a break above which the power-law slope is ~-2 and below which the slope is ~-1 (see UMP02 for additional discussion). In contrast to the broad-line targets, the best-fitting model for the soft-spectrum source Ark 564 seems to mimic the low-frequency breaks seen in low-state XRBs, those from the intermediate slope of -1 above the break to zero below it (consistent in shape to the low-frequency break in the doubly broken model fit to the NGC 3783 PSD). Alternatively, we caution the reader that soft-spectrum targets like Ark 564 may in fact exhibit fundamentally different variability characteristics in the 2–10 keV band from broad-line Seyfert 1 galaxies (see, e.g., Edelson et al. 2002), and the entire underlying broadband PSD shape may in fact be significantly different from low-state XRBs. The limited dynamic range of the present PSD for this target hinders this question. The low-frequency PSD flattening to zero slope in Ark 564 presents difficulty in solidifying the inviting analogy between soft-spectrum Seyfert 1 galaxies such as Ark 564 and high-state XRBs (which show $1/f$ noise down to frequencies of a few times 10^{-3} Hz; e.g., Churazov, Gilfanov, & Revnivstev 2001) because both types of systems are suspected of accreting at relatively high fractions of the Eddington limit (e.g., Pounds, Done, & Osborne 1995) and both show a steep energy spectrum ($\Gamma \sim 2.4$; e.g., Vaughan et al. 1999; Leighly 1999). Finally, what physical process is responsible for the variability? There are few specific models available, although some are discussed briefly in § 5.4.

5.3. *Correlations between Break Timescale, Luminosity, and Mass Estimates*

For the seven Seyfert 1 galaxies under consideration, Table 6 lists bolometric luminosity $L_{\rm bol}$, black hole mass estimate $M_{\rm BH}$, and PSD break timescale $T_{\rm (days)}$ from the singly broken power-law model fits (for NGC 3783, the high-frequency break from the doubly broken model fit is used). The timescale for MCG $-$6-30-15 is from the "high-frequency break" model used by UMP02. Bolometric luminosity is calculated using the mean bolometric correction of Padovani & Rafanelli (1988), $L_{\rm bol} = 27 L_{2\text{–}10\,\rm keV}$. It should be noted that for the soft-spectrum Seyfert 1 Ark 564, the 2–10 keV X-ray to bolometric luminosity conversion of Padovani & Rafanelli (1988) should be treated as a conservative lower limit because of the large EUV excesses present in soft-spectrum Seyfert 1 galaxies (see, e.g., Turner et al. 2002). The bolometric luminosity for MCG $-$6-30-15 is taken from Reynolds et al. (1997). All reverberation-mapped masses are taken from Kaspi et al. (2000), except for NGC 3516, which is from Wanders & Horne (1994). Ark 564 does not have a highly reliable reverberation-mapped mass estimate; the upper virial mass estimate is $\lesssim 8 \times 10^6$ $M_\odot$ by Collier et al. (2001), based on the lag between UV continuum flux and Lyα λ1316 variations. Reverberation mapping has not yet been done for MCG $-$6-30-15, but its black hole mass estimate can be derived as follows: Reynolds (2000) noted that the bulge luminosity of the host yields an approximate bulge mass of 3×10^9 $M_\odot$. The FWHM Hβ is 1700 km s^{-1} (Pineda et al. 1980), which, along with its steep energy index, nearly makes it consistent with the properties of most "officially" classified narrow-line Seyfert 1 galaxies such as Ark 564. Using the improved black hole mass–bulge relations from Wandel (2002; see their Figs. 3 and 4), for which narrow-line Seyfert 1 black

TABLE 6

TIMESCALE, BOLOMETRIC LUMINOSITY, AND BLACK HOLE MASS ESTIMATE

Target	PSD Break Timescale (days)	$L_{\rm bol}$ [log (ergs s^{-1})]	Black Hole Mass ($\times 10^7$ $M_\odot$)
Frl 9	>18.3	45.61	$8.3^{+2.5}_{-4.3}$
NGC 5548	>4.6	45.01	$9.4^{+1.7}_{-1.4}$
Ark 564	$7.3^{+11}_{-5.5}$	44.81	0.8
NGC 3783	$2.9^{+2.9}_{-1.4}$	44.65	$1.10^{+1.07}_{-0.98}$
NGC 3516	$5.8^{+5.8}_{-3.5}$	44.36	2.0 ± 0.3
MCG $-$6-30-15	$0.23^{+0.67}_{-0.12}$	44.24	0.1
NGC 4151	$9.2^{+37}_{-5.5}$	44.06	$1.20^{+0.83}_{-0.70}$

NOTE.—Targets are ranked by $L_{\rm bol}$. See text for details.

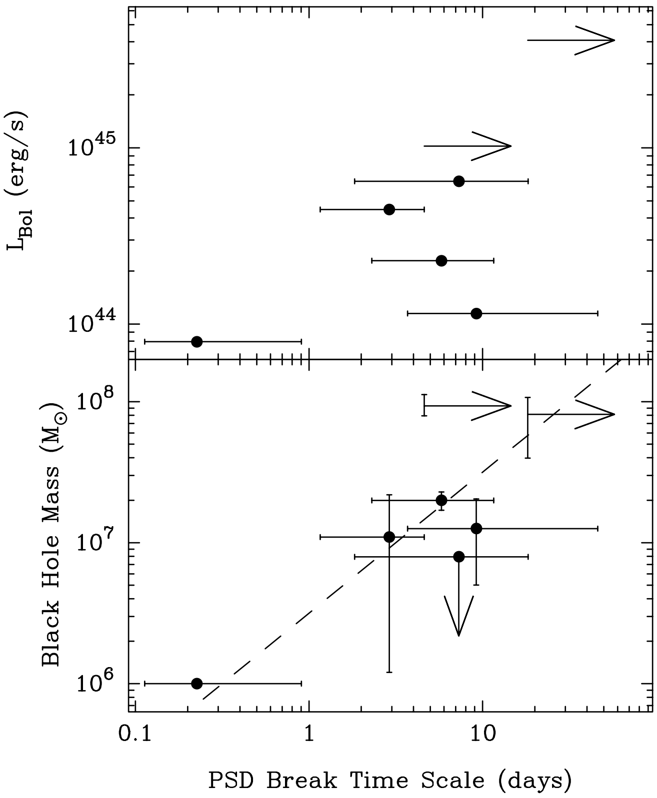

FIG. 12.—Bolometric luminosity and estimated black hole mass plotted against characteristic variability timescale (reciprocal of the PSD break frequency) from the singly broken power-law model fits (for NGC 3783, the high-frequency break from the doubly broken model fit is used; lower limits to timescale are shown for Frl 9 and NGC 5548). The timescale for MCG −6-30-15 is from UMP02. Masses are reverberation-mapping estimates from Kaspi et al. (2000) except for NGC 3516 (from Wanders & Horne 1994) and Ark 564 (rough reverberation estimate by Collier et al. 2001). MCG −6-30-15 does not have a reverberation mass estimate; see text for details. The dashed line denotes the linear mass-timescale relation $T_{\rm days} = M_{\rm BH}/10^{6.5}\ M_\odot$.

hole masses lie about an order of magnitude below those for broad-line AGNs and normal galaxies, the black hole mass for MCG −6-30-15 is likely to be of order $\sim 1 \times 10^6\ M_\odot$, the value adopted henceforth in this paper.

Figure 12 shows $L_{\rm bol}$ and black hole mass plotted versus timescale. For luminosity versus timescale (*top panel*), the Pearson correlation coefficient r is 0.49, with a probability P_r of obtaining that value of r by chance of 0.27 for seven points. The bottom panel of Figure 12 shows that there is an apparent correlation between mass and timescale, with $r = 0.79$, and $P_r = 3.3 \times 10^{-2}$ for seven points. It should be noted that for NGC 3783, the low-frequency PSD break from the doubly broken model fit is not consistent with the above correlation. When the singly broken model timescale is used for NGC 3783 (as opposed to the high-frequency break from the doubly broken fit), r decreases to 0.48 ($P_r = 0.27$ for seven points) in the luminosity-timescale plot, and r decreases to 0.78 ($P_r = 3.9 \times 10^{-2}$ for seven points) in the mass-timescale plot.

A more significant difference arises when we plot $L_{2-10\,{\rm keV}}$ against timescale, using the X-ray luminosity for MCG −6-30-15 from UMP02, where r drops to 0.27 ($P_r = 0.56$ for seven points). Finally, because the PSD break for MCG −6-30-15 was obtained from a fit by UMP02 where the high-frequency slope was fixed to −1 and fixing the low frequency to 0 results in a break timescale of 2.26 days, we note that using this timescale instead results in $r = 0.52$ ($P_r = 0.23$ for seven points) for the luminosity-timescale plot and $r = 0.62$ ($P_r = 0.14$ for seven points) for the mass-timescale plot.

The apparent correlation between mass and timescale seen in Figure 12, stronger than the luminosity-timescale relation, supports the validity of the reverberation-mapping method of black hole mass estimation; furthermore, one could speculate that mass may be more relevant than luminosity in governing a given Seyfert's X-ray timing properties. The mass-timescale correlation is consistent with the linear relation $T_{\rm (days)} = M_{\rm BH}/10^{6.5}\ M_\odot$, but this is certainly not conclusive with only seven objects spanning a narrow range of luminosity and black hole mass. The mass-timescale correlation and the similar shapes of the PSD breaks are consistent with a picture in which the PSDs of all the Seyfert 1 galaxies considered here have a similar, universal broadband PSD shape (that of low-state XRBs) in which the PSD breaks move toward lower temporal frequency as black hole mass increases. This is consistent with the expectation that compact accreting black hole systems with a relative larger black hole mass and larger Schwartzschild radius, $R_{\rm Sch}$, have a larger X-ray emission region, requiring a comparatively longer duration for the source to achieve a given amplitude of flux variability and longer characteristic variability timescales. This paradigm is manifested in findings of an anticorrelation between X-ray luminosity and excess variance, as measured over a fixed duration (Nandra et al. 1997; Turner et al. 1999; Markowitz & Edelson 2001).

It is also interesting to note that if one extrapolates the linear mass-timescale relation down to Cyg X-1's mass of 10 $M_\odot$, the inverse of the resulting timescale is 3.7 Hz, remarkably close to Cyg X-1's mean high-frequency break of 3.3 Hz, again supporting the notion of a common variability mechanism in both types of objects. This is also suggestive that there is only a small departure from linearity of the mass-timescale relation over 6–7 decades. Furthermore, this suggests that the PSD breaks detected are high-frequency breaks, supported by the similar changes in slope from ~ -2 to ~ -1 (with Ark 564 being an exception).

Finally, we note that the claim of a high-frequency break at $\sim 2 \times 10^{-3}$ Hz in the PSD of Ark 564 by Papadakis et al. (2002) does not fall anywhere near this mass-timescale relation; Papadakis et al. (2002) note this fact and consider the possibility that the break detected may not be indicative of black hole mass.

5.4. *Correlations between PSD Amplitude, Luminosity, and Mass Estimates*

Figure 13 shows the bolometric luminosity and black hole mass plotted against A, the PSD amplitude at the break (in P_f space) in the singly broken model fits (high-frequency break from the doubly broken fit for NGC 3783). Also included is MCG −6-30-15's break amplitude from UMP02, $A = 213 \pm 8$ Hz^{-1}. Under the assumption that it is a "low-frequency" break, that of Ark 564 is excluded. Although there are only six data points, there appears to be strong correlation between black hole mass and PSD break amplitude, with Pearson $r = 0.95$ ($P_r = 3.1 \times 10^{-3}$). There is a moderate correlation between $L_{\rm bol}$ and PSD break amplitude, with $r = 0.72$ ($P_r = 0.10$).

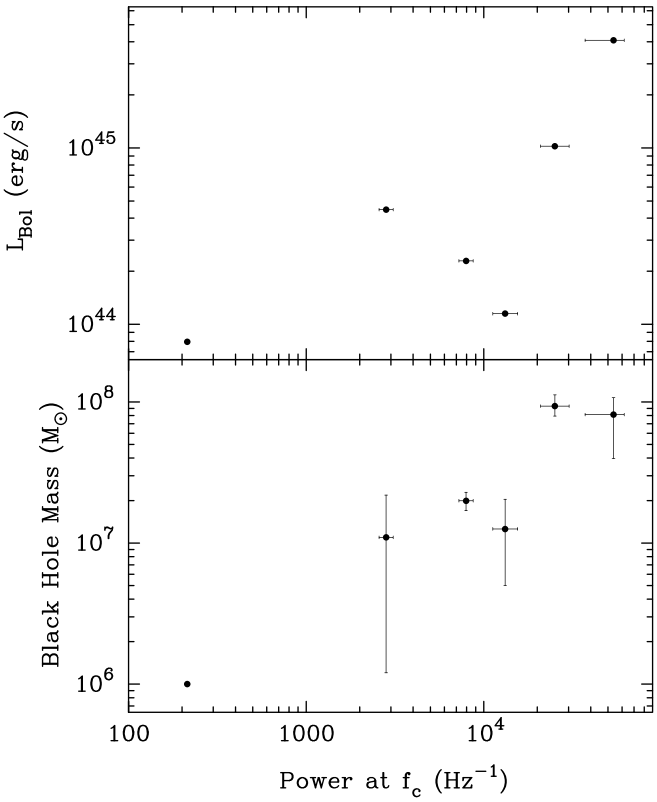

FIG. 13.—Bolometric luminosity and estimated black hole mass plotted against the amplitude of the best-fitting underlying PSD at the break frequency. The model fit and amplitude for MCG −6-30-15 are from UMP02.

These correlations reflect how the PSD, still assumed to have the same universal shape as low-state XRBs, moves not only downward in temporal frequency but also upward in power at the break frequency as black hole mass increases. In a sample of nine broad-line Seyfert galaxies (including all six broad-line Seyfert galaxies discussed thus far), Markowitz & Edelson (2001) saw that the dependence of long-term excess variance (measured over 300 days) on luminosity was much shallower than the dependence on short-term (1 day) excess variance. This indicated that the long-term excess variances likely probed down to temporal frequencies below targets' respective PSD breaks. As a given PSD moves toward lower temporal frequencies as black hole mass increases, the power level at the break must increase so that long-term excess variance stays similar. The above correlation arises mainly because the peak power in $f \times P_f$ space is broadly the same for all targets ($f \times P_f \sim 0.01$), similar to that of Cyg X-1, as discussed by, e.g., UMP02, not only strengthening the notion of similar variability mechanisms in Seyfert galaxies and XRBs but also implying similar numbers of varying X-ray–emitting regions.

5.5. *Testing Physical Timescales*

Since the observed cutoff is expected to relate to the physical process that generates the variability, one can explore the relevance of various physical processes to the origin of the X-ray variability by comparing physical timescale predictions to the measured PSD timescales. EN99 discuss the relevance of light-travel time effects and the orbital timescale for a standard α-disk (Shakura & Sunyaev 1973), comparing them to the PSD break observed in NGC 3516. EN99 note that for NGC 3516, and we note that for our Seyfert galaxies here, these timescales are both generally too short to be directly associated with the days-to-weeks PSD timescales. Additionally, the radial drift/viscous timescale is usually a few orders of magnitude longer than observed PSD timescales. However, the thermal and acoustic variation timescales for a thin disk (days to weeks given the putative black hole masses considered; Maraschi, Molendi, & Stella 1992; Treves, Maraschi, & Abramowicz 1988) are closest to the measured characteristic variability timescales. We hence speculate that the mechanism of X-ray variability may be tied to physical processes that incorporate thermal or acoustic thin-disk variations. If this is indeed the case, then the characteristic timescales and black hole mass estimates can be used to constrain the X-ray–emitting location. Assuming reasonable values for the scale height and viscosity, and assuming that the thin disk approximation holds over the entire radius range, all of the targets' acoustic and thermal timescales are consistent with the variable X-ray emission originating within $\sim 30 R_{\rm Sch}$.

However, more specific models can be considered. For instance, in the pulse avalanche model of Poutanen & Fabian (1999), the variable X-ray emission is produced in an inhomogeneous, stochastic system of magnetic flares inflating and detaching above the inner accretion disk, producing X-ray flares via inverse Compton scattering of softer photons, but with events occurring in correlated avalanches. The resulting light curves can yield doubly broken PSDs similar to those of low-state XRBs for appropriately tuned parameters, with a break between $f^{-\beta}$ noise and f^{-1} noise being associated with the longest timescale (days to weeks for the broad-line Seyfert 1 galaxies considered here) of an individual flare. A low-frequency PSD break from f^{-1} to white noise is associated with the duration of the avalanches. However, predicted flare durations are generally too short to be directly associated with PSD breaks.

Along another vein, the X-ray variability in the model of Lyubarski (1997) is caused by variations in the accretion flow (e.g., due to turbulence) propagating from large radii inward to the location of the X-ray corona. Such fluctuations in viscosity are dependent on the local viscous timescale, which decreases with decreasing radius. For standard thin disks, the viscous timescale is too long to be associated with the measured PSD breaks. However, if the accretion flow is geometrically thick, such as an advection-dominated accretion flow (ADAF; Narayan & Yi 1994) or a radiation-supported thick disk (e.g., see Abramowicz 1988; Treves, Maraschi, & Abramowicz 1988), the viscous timescale tends toward the thermal timescale. Therefore, the PSD breaks seen might plausibly correspond to a viscous timescale in an ADAF or radiation-supported thick disk.

6. CONCLUSIONS

We have systematically constructed high-quality broadband PSDs for a sample of six Seyfert 1 galaxies. These high-quality PSDs cover exceptional dynamic ranges, continuously spanning up to or beyond 3–4 orders of magnitude in temporal frequency. We use the Monte Carlo technique of UMP02 to determine adequate errors on each binned PSD point and to account for distortion effects, and we characterize the underlying PSD shape to look for low-frequency flattening below a characteristic break frequency. Four targets (Ark 564, NGC 3783, NGC 3516, and NGC 4151) show significant evidence for low-frequency flattening, with characteristic variability timescales in the range of several to tens of days. For the two most massive and luminous targets in the sample (Frl 9 and NGC 5548), we expect that continued long-term monitoring and extending the PSD to probe lower frequencies will confirm their break frequencies, which are the lowest in the sample. The low-frequency flattening seen in these objects is remarkably similar to what is seen in low-state X-ray binary PSDs, strengthening the argument that similar emission processes occur in both types of compact accreting systems, spanning a factor of $\sim 10^6$ to 10^7 in luminosity and putative black hole mass.

All of the PSDs studied are consistent in shape with at least portions of low-state XRB PSDs. The finding of two breaks in the PSD of NGC 3783 is only tentative, but it still heralds a new era in Seyfert PSD analysis: those PSDs derived from *EXOSAT* data generally lacked the temporal frequency range to reveal even a single break, and the access to long timescales afforded by *RXTE* allowed detection of a single break (EN99; Pounds et al. 2001; UMP02; this work). However, as double power-law breaks are routinely detected in XRB PSDs, only Seyfert PSDs that also show two breaks will exhibit the most direct and convincing evidence for a link between the two classes of systems. More long-term monitoring is therefore crucial for locating low-frequency PSD breaks.

The PSD break frequencies detected are model dependent, but when compared to reverberation-mapped black hole masses, they are consistent with a linear mass-timescale relation that extends not only throughout the Seyfert range but down to the mass and PSD timescale of Cyg X-1, providing even further support for similar variability processes in Seyfert galaxies and XRBs. The correlation, however, is hampered by small-number statistics, and more accurate black hole mass estimates for Ark 564 and MCG −6-30-15 are needed to clarify the situation; this is especially important for MCG −6-30-15 since its mass estimate is very crude, yet it is used to anchor the low-mass end of the black hole mass–timescale relation shown in Figure 12.

It is encouraging to note that this agreement between X-ray variability timescale and reverberation mapping arises despite numerous caveats and assumptions in both analysis methods (e.g., the assumption of broad-line emission clouds being on Keplerian orbits; Peterson & Wandel 1999), each of which is expected to probe different regions of the central engine.

Finally, we draw the reader's attention back to Figure 11 because we believe such diagrams will play a large role in future Seyfert 1 PSD analysis. It is a plot of $f \times P_f$ as a function of f in model space, while most previous PSD plots were of P_f as a function of f in data space. In this regard, it mimics the "unfolded" (model-space) νF_ν plots of early X-ray energy spectral analyses. That was done to give the clearest possible visual picture of the intrinsic energy spectrum itself, undistorted by the vagaries of the response matrix of a particular detector. Likewise, this plot gives the clearest possible picture of the underlying PSD, after removal of the distortions unique to the particular sampling pattern employed. Further, just as a peak in the νF_ν plots indicated a region of maximum luminosity per decade of frequency, so a well-defined peak in the $f \times P_f$ PSD plot occurs in the temporal frequency band at which most of the variability power is produced. These data indicate that the "characteristic variability timescales" of these Seyfert 1 galaxies are typically of order a few days.

Establishing that breaks are a systematic feature of their PSDs represents a milestone in the description of Seyfert 1 X-ray variability. Here too there is analogy with the early energy spectral studies: the low-resolution energy spectra from early missions (e.g., *Ariel 5*) were well modeled as "canonical" $\Gamma \sim 1.7$ power laws, but a critical breakthrough came when Wilkes & Elvis (1987) unambiguously established the existence of a significant departure, the "soft excess," from the *Einstein* data. As the spectral resolution and bands improved over the following 15 yr, many more spectral features have been found (e.g., narrow absorption lines that make up the "warm absorber," the iron Kα fluorescence line, the Compton reflection component). Now this work has clearly established the pervasiveness of breaks in Seyfert 1 PSDs that were modeled as simple power laws in previous, lower dynamic range PSDs. We cannot be certain that this is strictly a broken power law; many other parameterizations are of course possible. We can be fairly confident, however, that the current description of Seyfert 1 PSDs will be refined and eventually overturned, just as the "canonical" energy spectral power law was 15 yr ago, as we further probe long timescales with *RXTE* and short timescales with *XMM-Newton* and the flight of Lobster-ISS[12] starting in 2009 increases the number of Seyfert 1 PSDs more than tenfold.

The authors thank the anonymous referee for a very detailed reading of the manuscript. The authors also acknowledge the dedication of the entire *RXTE* mission team, especially Evan Smith, for scheduling the long-term observations so evenly all these years. A. M. thanks Rick Paik-Schoenberg of the UCLA Statistics Department for useful discussions on spectral windowing. This work has made use of data obtained through the High Energy Astrophysics Science Archive Research Center Online Service, provided by the NASA Goddard Space Flight Center, the TARTARUS database, which is supported by Jane Turner and Kirpal Nandra under NASA grants NAG 5-7385 and NAG 5-7067, and the NASA/IPAC Extragalactic Database, which is operated by the Jet Propulsion Laboratory, California Institute of Technology, under contract with the National Aeronautics and Space Administration. A. M. and R. E. acknowledge financial support from NASA grant NAG 5-9023. R. E. G. acknowledges financial support from NASA grant NAG 5-9902.

[12] See http://www.src.le.ac.uk/lobster.

REFERENCES

Abramowicz, M. 1988, Adv. Space Res., 8, 151
Belloni, T., & Hasinger, G. 1990, A&A, 230, 103
Brillinger, D. 1981, Time Series: Data Analysis and Theory (2d ed.; San Francisco: Holden-Day)
Churazov, E., Gilfanov, M., & Revnivstev, M. 2001, MNRAS, 321, 759
Collier, S., et al. 2001, ApJ, 561, 146
Done, C., Madejski, G., Mushotzky, R., Turner, T. J., Koyama, K., & Kunieda, H. 1992, ApJ, 400, 138
Edelson, R., & Nandra, K. 1999, ApJ, 514, 682 (EN99)
Edelson, R., Turner, J., Pounds, K., Vaughan, S., Markowitz, A., Marshall, H., Dobbie, P., & Warwick, R. 2002, ApJ, 568, 610
Fabian, A. C., Nandra, K., Reynolds, C. S., Brandt, W. N., Otani, C., Tanaka, Y., Inoue, H., & Iwasawa, K. 1995, MNRAS, 277, L11
Green, A., McHardy, I., & Lehto, H. 1993, MNRAS, 265, 664
Hayashida, K., Miyamoto, S., Kitamoto, S., & Negoro, H. 1998, ApJ, 500, 642
Herrero, A., Kudritzki, R., Gabler, R., Vilchez, J., & Gabler, A. 1995, A&A, 297, 556
Kaspi, S., Smith, P., Netzer, H., Maoz, D., Jannuzi, B., & Giveon, U. 2000, ApJ, 533, 631
Kaspi, S., et al. 2001, ApJ, 554, 216
———. 2002, ApJ, 574, 643
Lawrence, A., & Papadakis, I. 1993, ApJ, 414, L85
Lawrence, A., Watson, M., Pounds, K., & Elvis, M. 1987, Nature, 325, 694
Leighly, K. 1999, ApJS, 125, 317
Lyubarski, Y. 1997, MNRAS, 292, 679
Maraschi, L., Molendi, S., & Stella, L. 1992, MNRAS, 255, 27
Markert, T., Canizares, C., Dewey, D., McGuirk, M., Pak, C., & Schattenburg, M. 1994, Proc. SPIE, 2280, 168
Markowitz, A., & Edelson, R. 2001, ApJ, 547, 684
McHardy, I. 1988, Mem. Soc. Astron. Italiana, 59, 239
McHardy, I., & Czerny, B. 1987, Nature, 325, 696
Nandra, K., George, I., Mushotzky, R. F., Turner, T. J., & Yaqoob, T. 1997, ApJ, 476, 70
Nandra, K., & Papadakis, I. 2001, ApJ, 554, 710
Narayan, R., & Yi, I. 1994, ApJ, 428, L13
Nousek, J., et al. 1998, Proc. SPIE, 3444, 225
Nowak, M., Vaughan, B., Wilms, J., Dove, J., & Begelman, M. 1999a, ApJ, 510, 874
Nowak, M., Wilms, J., & Dove, J. 1999b, ApJ, 517, 355
Oppenheim, A., & Schafer, R. 1975, Digital Signal Processing (Englewood Cliffs: Prentice-Hall)
Padovani, P., & Rafanelli, P. 1988, A&A, 205, 53
Papadakis, I., Brinkmann, W., Negoro, H., & Gliozzi, M. 2002, A&A, 382, L1
Papadakis, I., & Lawrence, A. 1993a, MNRAS, 261, 612
———. 1993b, Nature, 361, 233
Papadakis, I., & McHardy, I. 1995, MNRAS, 273, 923
Papadakis, I., Nandra, K., & Kazanas, D. 2001, ApJ, 554, L133
Peterson, B., & Wandel, A. 1999, ApJ, 521, L95
Piccinotti, G., et al. 1982, ApJ, 253, 485
Pineda, F. J., Delvaille, J. P., Schnopper, H. W., & Grindlay, J. E. 1980, ApJ, 237, 414
Plucinsky, P., et al. 2003, Proc. SPIE, 4851, 89
Pounds, K., Done, C., & Osborne, J. 1995, MNRAS, 277, L5
Pounds, K., Edelson, R., Markowitz, A., & Vaughan, S. 2001, ApJ, 550, L15
Poutanen, J., & Fabian, A. 1999, MNRAS, 306, L31
Priestley, M. 1981, Spectral Analysis and Time Series (London: Academic)
Reynolds, C. 2000, ApJ, 533, 811
Reynolds, C., Ward, M., Fabian, A., & Celotti, A. 1997, MNRAS, 291, 403
Schurch, N., & Warwick, R. 2002, MNRAS, 334, 811
Shakura, N. I., & Sunyaev, R. A. 1973, A&A, 24, 337
Strüder, L., et al. 2001, A&A, 365, L18
Sunyaev, R., & Revnivtsev, M. 2000, A&A, 358, 617
Swank, J. 1998, Nucl. Phys. B Proc. Suppl., 69, 12
Tanaka, Y., et al. 1995, Nature, 375, 659
Timmer, J., & König, M. 1995, A&A, 300, 707
Treves, A., Maraschi, L., & Abramowicz, M. 1988, PASP, 100, 427
Turner, M. J. L., et al. 2001, A&A, 365, L27
Turner, T. J., George, I. M., Nandra, K., & Turcan, D. 1999, ApJ, 524, 667
Turner, T. J., et al. 2002, ApJ, 568, 120
Uttley, P., & McHardy, I. 2001, MNRAS, 323, L26
Uttley, P., McHardy, I., & Papadakis, I. 2002, MNRAS, 332, 231 (UMP02)
van der Klis, M. 1997, in Statistical Challenges in Astronomy II, ed. G. J. Babu & E. D. Feigelson (New York: Springer), 321
Vaughan, S., Pounds, K., Reeves, J., Warwick, R., & Edelson, R. 1999, MNRAS, 308, L34
Wandel, A. 2002, ApJ, 565, 762
Wanders, I., & Horne, K. 1994, A&A, 289, 76
Wilkes, B., & Elvis, M. 1987, ApJ, 323, 243
Wilms, J., Nowak, M., Dove, J., Fender, R., & di Matteo, T. 1999, ApJ, 522, 460